JGR Solid Earth

RESEARCH ARTICLE
10.1029/2023JB026352

Hypocenter-Based 3D Imaging of Active Faults: Method and Applications in the Southwestern Swiss Alps

Sandro Truttmann[1], **Tobias Diehl**[2], **and Marco Herwegh**[1]

[1]Institute of Geological Sciences, University of Bern, Bern, Switzerland, [2]Swiss Seismological Service, ETH Zürich, Zürich, Switzerland

Key Points:

- We present a novel approach that uses relocated hypocenters to image 3D geometries and instabilities of active faults
- Application to two earthquake sequences in the Southwestern Swiss Alps provides detailed insights into these strike-slip faults systems
- This study documents the dynamics of earthquake-migration processes across stepover faults at high resolution

Supporting Information:

Supporting Information may be found in the online version of this article.

Correspondence to:

S. Truttmann,
sandro.truttmann@unibe.ch

Citation:

Truttmann, S., Diehl, T., & Herwegh, M. (2023). Hypocenter-based 3D imaging of active faults: Method and applications in the Southwestern Swiss Alps. *Journal of Geophysical Research: Solid Earth*, *128*, e2023JB026352. https://doi.org/10.1029/2023JB026352

Received 1 JAN 2023
Accepted 29 MAY 2023

Author Contributions:

Conceptualization: Sandro Truttmann, Tobias Diehl, Marco Herwegh
Formal analysis: Sandro Truttmann, Tobias Diehl
Funding acquisition: Marco Herwegh
Investigation: Sandro Truttmann, Tobias Diehl
Methodology: Sandro Truttmann, Tobias Diehl, Marco Herwegh
Project Administration: Marco Herwegh
Software: Sandro Truttmann
Supervision: Marco Herwegh
Visualization: Sandro Truttmann

Abstract Despite the fact that earthquake occurrence can be strongly influenced by the architecture of pre-existing faults, it remains challenging to obtain information about the detailed subsurface geometries of active fault systems. Current geophysical methods for studying such systems often fail to resolve geometrical complexities at sufficiently high spatial resolutions. In this work, we present a novel method for imaging the detailed 3D architectures of seismically active faults based on high-precision hypocenter catalogs, using nearest neighbor learning and principal component analysis. The proposed approach enables to assess variations in fault instabilities and kinematics. We apply the method to the relatively relocated St. Léonard (max. $M_L = 3.2$) and Anzère (max. $M_L = 3.3$) microearthquake sequences in the Southwestern Swiss Alps, revealing strike-slip fault systems with interconnecting stepovers at depths of 3–7 km and lengths ranging from 0.5 to 2 km. In combination with additional information about fault instabilities and kinematics, we observe significantly reduced earthquake migration velocities and fault locking processes within the stepovers. Understanding such processes and their role in the propagation of strain across stepovers is of great relevance, as these structures can potentially limit earthquake ruptures but also represent possible locations for the nucleation of larger ruptures. Our proposed method is expected to be broadly useful for further applications such as monitoring hydraulic fracture stimulations or geothermal exploration of natural, fluid-bearing faults. Conducting similar high-resolution spatiotemporal analyses of microseismic sequences has the potential to greatly enhance our comprehension of how the 3D fault architecture impacts seismogenic fault reactivation.

Plain Language Summary Earthquakes commonly occur on planar geological structures, called faults. Profound knowledge of the presence and geometries of earthquake-generating faults is crucial to understand the regional earthquake hazards. Especially for regions with distributed and rather small earthquakes, it is however challenging to detect such faults, because of the fact that these faults often do not reach the surface. Here, we present a new method that uses the locations of small earthquakes to resolve the geometries of earthquake-generating faults at depth. This is only possible due to the recent advances in earthquake location methods, which can reduce the uncertainties of the locations from the kilometers down to some tens of meters for precise measurements. With our method, we image the complex geometries of two fault systems in the Southwestern Swiss Alps at high resolution. The knowledge obtained by applying our method cannot only help to detect previously unknown, potentially hazardous earthquake-generating faults but might also improve our understanding of earthquake processes in general.

1. Introduction

Earthquakes typically occur along pre-existing tectonic structures, such as plate boundaries or intraplate fault zones. These fault zones often have complex architectures, consisting of multiple interconnected, non-planar, and localized high-strain zones. The high-strain zones are embedded in numerous secondary small-scale faults and fractures that form the surrounding damage zone (e.g., Faulkner et al., 2010; Perrin et al., 2016; Wibberley et al., 2008). The geometrical complexities and segmentation of such fault zones significantly influence the local stress field, directly affecting nucleation, propagation, termination, and source mechanisms of earthquakes (Barka & Kadinsky-Cade, 1988; Kaven & Pollard, 2013; Kinoshita et al., 2019; Lay & Kanamori, 1981; Legrand et al., 2020; Manighetti et al., 2007, 2009; Romanet et al., 2018; Segall & Pollard, 1980). In many studies, seismogenic faults are, however, approximated as simplified planar structures, mostly due to the limited knowledge of the detailed fault geometries in the subsurface. Hence, a significant challenge is to identify and distinguish the complex fault architectures of seismically active faults at depth.

Writing – original draft: Sandro Truttmann
Writing – review & editing: Tobias Diehl, Marco Herwegh

The detection of seismically active faults with geophysical methods is demanding, especially in regions characterized by low strain rates, spatially distributed seismicity, and diffuse fault patterns. Active geophysical methods, such as reflection seismics, are limited by (a) the difficulty of detecting subvertical faults, (b) the absence of reflectors in crystalline basement rocks, and (c) the lack of direct information on whether or not a fault is active (e.g., Hajnal et al., 1996; Lynn & Deregowski, 1981). Thus, there is a need for methods to resolve active faults in such regions. Since successive earthquakes often nucleate along the same fault systems, the alignment of hypocenters might be used to reconstruct the geometries of active faults (e.g., Ouillon et al., 2008). We here introduce the term "hypocenter-based 3D imaging of active faults," which refers to the imaging of active faults using earthquake hypocenter locations. The large uncertainties in hypocenter locations, particularly in focal depth, have, however, limited this approach in the past. Recent advances in absolute (e.g., Diehl, Kissling, et al., 2021; Husen et al., 2003; Lomax et al., 2000, 2014; Lomax & Savvaidis, 2022; Theunissen et al., 2018) and relative earthquake relocation techniques (e.g., Console & Di Giovambattista, 1987; Hauksson & Shearer, 2005; Trugman & Shearer, 2017; Waldhauser & Ellsworth, 2000), as well as enhanced earthquake detection methods (e.g., Chamberlain et al., 2017; Gibbons & Ringdal, 2006; Herrmann et al., 2019; Ross et al., 2017; Schaff & Waldhauser, 2010; Shelly et al., 2006; Simon et al., 2021) significantly improved the hypocenter catalogs in the last years. In ideal cases (dense monitoring network, high sampling rates, impulsive onsets, high waveform similarities, etc.), relative location uncertainties on the order of ten to hundred meters can be achieved (e.g., Deichmann & Giardini, 2009; Simon et al., 2021; Trugman & Shearer, 2017; Valoroso et al., 2013; Waldhauser & Ellsworth, 2000). This increase in quality and quantity of earthquake catalogs opens new possibilities in imaging active faults based on hypocenter locations as described, for example, by Ross et al. (2019).

Previous approaches to derive geometries of active faults from hypocenter locations were mainly based on clustering algorithms such as single link (Frohlich & Davis, 1990), Gaussian mixture (Meyer et al., 2019; Ouillon & Sornette, 2011), *k*-means (Ouillon et al., 2008; Wang et al., 2013), DBSCAN (Brunsvik et al., 2021; Skoumal et al., 2019), agglomerative clustering (Kamer et al., 2020), RANSAC (Kaven & Pollard, 2013; Skoumal et al., 2019) or waveform similarity measures (Deichmann et al., 2014; Petersen et al., 2021). Spatial clustering allocates each hypocenter to a certain seismogenic fault system according to the defined clustering parameters, which often requires critical assumptions such as the expected number of faults (Ouillon et al., 2008; Wang et al., 2013) or splitting and merging criteria (Kamer et al., 2020; Meyer et al., 2019; Ouillon & Sornette, 2011). The associated geometrical fitting of the seismogenic fault networks is often oversimplified by the assumption of rectangular planes (Meyer et al., 2019; Ouillon et al., 2008; Ouillon & Sornette, 2011; Petersen et al., 2021; Wang et al., 2013). Both Kaven & Pollard (2013) and Brunsvik et al. (2021) went beyond the use of simple planar structures and modeled the fault systems by fitting curved surfaces. Kamer et al. (2020) used a different approach to overcome this problem by representing the fault geometries as 3D kernels. Moreover, many existing fitting methods do not incorporate additional constraints such as location errors (Deichmann et al., 2014; Ouillon & Sornette, 2011; Petersen et al., 2021), earthquake magnitudes (Brunsvik et al., 2021; Kaven & Pollard, 2013; Ouillon et al., 2008) or focal mechanisms (Kamer et al., 2020; Kaven & Pollard, 2013). Especially the latter is critical, since independent constraints from the focal mechanisms facilitate the discrimination of the main fault with consistent slip modes from the surrounding damage zones or interconnecting fault structures.

In this study, we make use of high-precision microearthquake catalogs derived from relative double-difference hypocenter relocations. The 3D geometries of active fault networks as well as their likelihood for reactivation and kinematics at depth are derived from these high-precision catalogs. We hereby also consider respective relative location uncertainties and constraints from high-quality focal mechanisms. To image active fault networks in 3D, we implemented a Monte Carlo based algorithm in Python that uses nearest-neighbor learning and principal component analysis (PCA). After the description of the methodology and its benchmarking with a synthetic data set, we apply the method to two relatively relocated microearthquake sequences, which occurred in the Southwestern Swiss Alps between 2014 and 2021.

2. Methods

2.1. Double-Difference Relative Relocation and Focal Mechanisms

The significance of fault geometries reconstructed from earthquake locations crucially depends on the precision of the used hypocenters solutions. To derive such high-precision locations, we applied the well-established hypoDD double-difference (DD) relative relocation approach of Waldhauser & Ellsworth (2000). This approach

combines delay times measured from manual phase picks and cross-correlation (CC) of similar waveforms, thus also weighting the waveform similarities of the events (Waldhauser & Ellsworth, 2000). The initial locations for the DD procedure in this study are taken from the improved absolute locations of Diehl, Kissling, et al. (2021), derived from a probabilistic relocation in combination with new 3D P and S wave velocity models. As documented by Diehl, Kissling et al. (2021) and Lee et al. (2023), these locations achieve sub-kilometer accuracy in terms of absolute locations for well-constrained hypocenters. The 1D P and S wave velocity models used for the DD relocation correspond to the regional 1D models of Diehl, Kissling et al. (2021). As demonstrated by Diehl, Kissling et al. (2021), this combination of 3D regional velocity models for absolute location and 1D regional models for subsequent DD relocation leads to relative hypocenters (as well as cluster centroids) almost identical to the ones obtained with local 1D velocity models. The computation of CC-based delay times and associated quality control follows the procedure described in Diehl et al. (2017). The original recording sampling rate of the seismograms varies between 120 and 250 Hz. Prior to the cross-correlation, seismograms are resampled with a sample interval of 1 ms and band passed in the frequency range of 1–20 Hz using a second-order filter. The cross-correlation is performed in the time domain, using a moving-window approach with a sample interval of 1 ms. P phases are cross-correlated on vertical (Z) components, S phases on rotated transverse (T) components. We used the damped least-square inversion solver of hypoDD for several sets of inversions. Following the procedure proposed by Waldhauser & Ellsworth (2000), we incrementally increase the weight of the CC data from one set of inversions to the next, while incrementally decreasing the weight of the manual picked data. At the same time, we successively reduce the maximum inter-event distance and residual thresholds of both data types. The complete sets of used hypoDD parameters are provided as control files in the data repository (Truttmann et al., 2023a). Formal relative relocation errors in x, y, and z directions are estimated with a statistical resampling approach following the procedure proposed by Waldhauser & Ellsworth (2000), which results in error values corresponding to three standard deviations (3σ). Our resampling approach is described in detail in Text S1 in Supporting Information S1. The DD procedure was applied to relocate two earthquake sequences in the Southwestern Swiss Alps, one of the seismically most active regions in the Alps. In these sequences, we only considered events that were detected by standard STA/LTA trigger methods as implemented in the monitoring system of the Swiss Seismological Service (SED). These standard detection methods achieve a magnitude of completeness (M_C) of about 0.8 or smaller in this region (e.g., Diehl, Clinton, et al., 2021; Lee et al., 2023). Even smaller events detected with additional methods below the standard M_C, as described, for example, by Simon et al. (2021), are not included in this study.

In addition, we use high-quality first-motion focal mechanisms associated with the two earthquake sequences. All mechanisms were derived with the method described, for example, by Diehl, Clinton, et al. (2021). This method uses manually determined P wave polarities and calculates the corresponding take-off angles from 3D P wave models using the NonLinLoc algorithm (Lomax et al., 2000, 2014). The first-motion mechanism is then determined with the HASH algorithm (Hardebeck & Shearer, 2002). Only solutions with a unique type of mechanism, defined by the maximum angular difference (cut-off angle parameter of 30°), are considered. For each mechanism, HASH computes the preferred solution (black fault planes in Figures S1 and S2 in Supporting Information S1) from the average of possible solutions (set of gray fault planes in Figures S1 and S2 in Supporting Information S1). The possible solutions are calculated using a grid spacing of 2° and also consider potential errors in the first-motion polarities as described by Hardebeck & Shearer (2002).

2.2. Hypocenter-Based Imaging of Active Faults

In the following sections, we present the methodology of the developed approach that performs the automated hypocenter-based imaging of active faults, resolving geometries, fault instabilities, and kinematics using the previously described catalogs of relative locations and focal mechanisms. The processing steps are summarized in Figure 1.

2.2.1. Fault Network Reconstruction

In a first step, the relocated hypocenters are imported (Figure 1a). Each hypocenter is then randomly shifted within its relocation errors using a normal distribution for a user-defined number of Monte Carlo iterations n_{MC} (Figure 1b). This step results in a Monte Carlo data set with a point cloud around each initial hypocenter, with the highest density at the initial hypocenter and decreasing densities toward the edges of the error ellipsoid. Note that the choice of n_{MC} depends on the magnitude of the relative relocation errors and should be chosen large enough so that the hypocenter locations represent a normal distribution. This choice can be assessed by investigating the

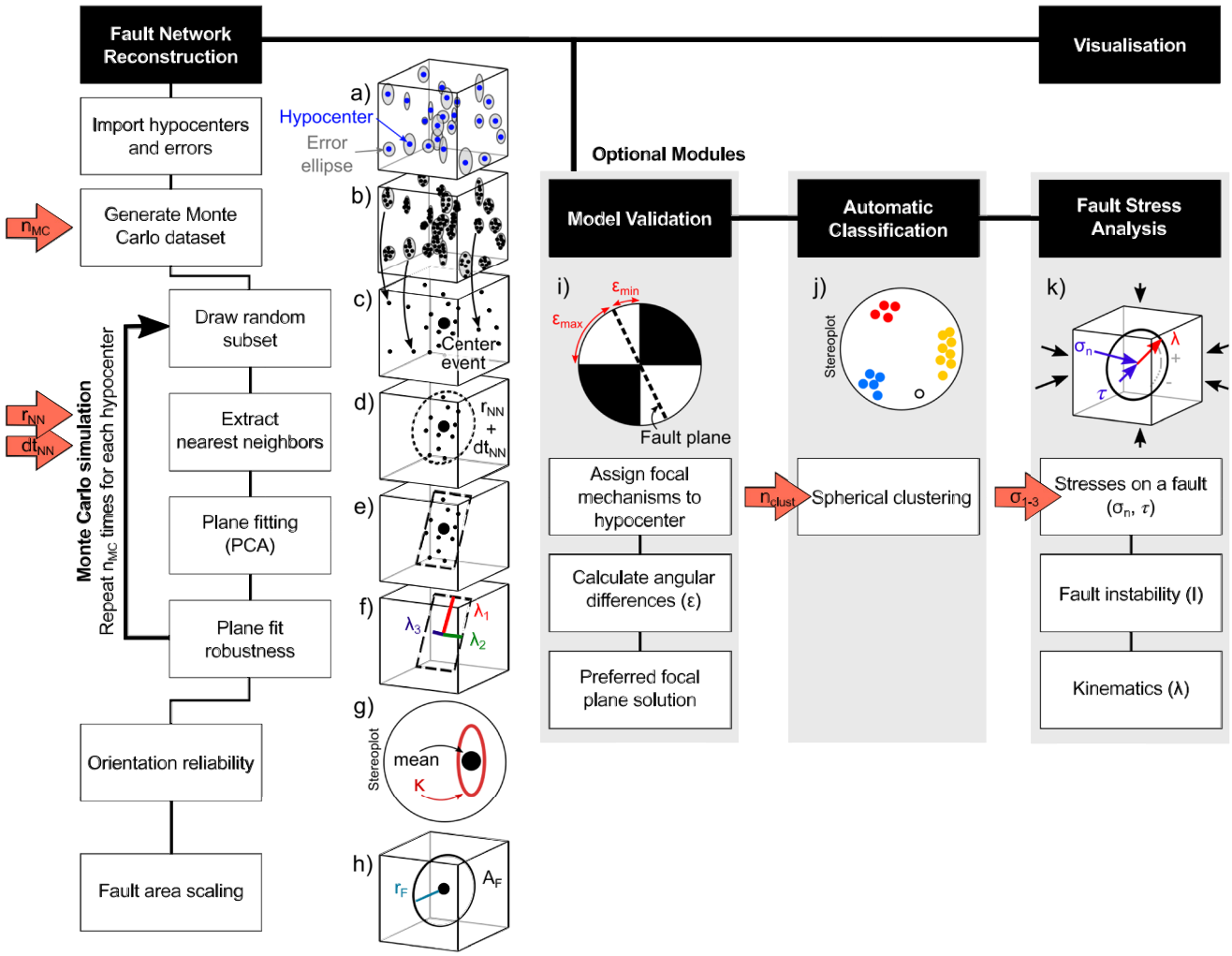

Figure 1. Flowchart that schematically illustrates the five main modules presented in the methods section. The red arrows mark different user-defined input parameters. The visualization module creates interactive 3D fault-network models using Plotly (Plotly Technologies, 2015).

distribution of the hypocenter locations for different values of n_{MC} (Figure S3 in Supporting Information S1). The Monte Carlo data set is used to calculate a set of fault-plane orientations for each earthquake with the following steps: (a) A subset of hypocenters with one randomly sampled point for each initial hypocenter is selected from the Monte Carlo data set (Figure 1c). (b) For the defined center event, the nearest neighbors of this subset within the user-defined search radius (r_{NN}) and search time (dt_{NN}) are extracted with the nearest-neighbor learning tool from scikit-learn (Pedregosa et al., 2011) (Figure 1d). (c) If more than five neighboring events are found, a best-fit plane orientation is calculated using PCA on the spatial covariance matrix of the extracted neighbors (Shakarji, 1998) (Figure 1e). Solving this eigenvalue problem yields the three eigenvectors, which correspond to the directional cosine vectors. The eigenvector belonging to the smallest eigenvalue λ_3 represents the plane's normal, whereas the perpendicular directions of λ_1 and λ_2 lie within the plane. (d) The eigenvalues λ_2 and λ_3 are used in a next step to assess the plane-fit robustness following the suggestions of Jones et al. (2016) (Figure 1f). To ensure that the nearest neighbors are not simply collinear but form a plane, fits with λ_2 smaller than the squared mean relocation error are rejected. To ensure planarity, only fits with λ_2 more than five times larger than λ_3 are accepted. Planes not fulfilling these criteria are not considered for further analysis and are rejected. (e) These plane-fit calculations are then repeated for each hypocenter and for all n_{MC} iterations. The Monte Carlo simulations therefore result in a multitude of fault orientations for each hypocenter.

Directional statistics are then used to evaluate the variability of these orientations for each hypocenter (Figure 1g). Only events for which more than 80% of the n_{MC} simulations resulted in a robust plane fit are considered for further

analysis. Under the assumption of an underlying Bingham distribution, the five-parameter Fisher-Bingham distribution (FB_5) from Kent (1982) can be used to fit the data (Borradaile, 2003; Mardia & Jupp, 2000). For this step, the implementation of the FB_5 distribution from Yuan (2021) yields the mean fault-plane orientation. The dimensionless concentration parameter κ from the FB_5 distribution is defined here as an orientation reliability parameter, where large κ values indicate more concentrated distributions and thus more reliable orientations.

The fact that the ruptured fault area scales with the released energy during an earthquake allows for first-order approximation of the rupture area from empirical scaling relationships based on the measured magnitude (e.g., Leonard, 2010, 2014; Wells & Coppersmith, 1994) (Figure 1h). The local magnitude M_L has first to be translated to the moment magnitude M_w. We use the empirical scaling laws of Goertz-Allmann et al. (2011), which are based on earthquakes in Switzerland. The rupture area A_F is then approximated with the empirical scaling law from Leonard (2014):

$$M_W = a + b * \log(A_F) \tag{1}$$

Values proposed for strike-slip earthquakes in stable continental regions of $a = 4.18$ and $b = 1$ are used in this study. Assuming a circular rupture plane, A_F can be translated into the rupture radius r_F. In conclusion, we obtain a fault-plane orientation and a rupture area for each earthquake.

2.2.2. Model Validation

As proposed by Wang et al. (2013), we assess the validity of the 3D fault-network model by comparing the calculated fault-plane orientations with the two nodal planes of the focal mechanism of the respective earthquake event. Since the focal mechanisms used in this study are based on first-motion polarities of the P wave, they provide an independent constraint on the orientation of the active plane. The focal mechanisms are loaded from a separate catalog and associated with the corresponding hypocenters by matching the origin time, hypocenter location, and magnitude. Subsequently, the angular differences ε between the fault-plane orientation and the two nodal planes of the focal mechanism are calculated. The nodal plane with the smaller angular difference ε_{min} is defined as the preferred solution. The angular difference ε_{min} describes the misfit in orientation between the calculated fault plane and the preferred nodal plane of the focal mechanism in degrees (Figure 1i). Assuming that the focal mechanisms are well constrained, smaller values of ε_{min} indicate higher reliability of the modeled fault network. As described in more detail in Section 4.2, the model validation module can be used to determine the optimal values of the input parameters r_{NN} and dt_{NN}.

2.2.3. Automatic Classification

To facilitate the structural interpretation of the derived fault model, we include a classification scheme that groups the earthquakes based on their fault orientations (Figure 1j). For this classification, the normal vectors of each fault plane are clustered on the unit sphere, using a soft-assigned mixture of von Mises-Fisher distributions (Banerjee et al., 2005). The number of expected clusters n_{clust} must be defined by the user. However, this choice does not affect the overall fault network imaging procedure. Since the poles of subvertical planes lie on the edge of the stereonet, spherical clustering might lead to erroneous results for such data sets because vertical faults with opposite dip directions appear to be disconnected. Therefore, the poles of subvertical fault systems have to be rotated toward the center of the stereonet before applying the spherical clustering. The automatic classification scheme results in different classes of faults, based on their distinctive orientations.

2.2.4. Fault Stress Analysis

The method further provides the option to estimate the likelihood for slip and the expected kinematics of each earthquake under the assumption of a uniform stress field in the vicinity of the imaged fault structure. The stresses on a fault depend solely on the applied effective principal stress and the respective fault orientation (e.g., Bott, 1959; Jaeger & Cook, 1979). We implement the tensor method described by Stein & Wysession (2003) to calculate the effective normal (σ_n) and shear tractions (τ). The ratio between the effective normal and shear tractions defines whether a fault is prone to slip or not. Similar to the slip tendency defined by Morris et al. (1996), the fault instability parameter I can be used to assess the likelihood of a cohesionless fault to slip reactivation, yielding values between 0 (most stable) and 1 (most unstable) (Vavryčuk et al., 2013). It is defined as:

$$I = \frac{\tau - \mu(\sigma_n - \sigma_1)}{\tau_c - \mu(\sigma_c - \sigma_1)} \tag{2}$$

where τ_c and σ_c are the shear and effective normal traction on a hypothetical, optimally oriented fault in a given stress field, and σ_n, respectively τ represent the effective normal and shear tractions on the fault plane of interest. Since Equation 2 is independent of absolute stress magnitudes, the scaling of the reduced stress tensor to $\sigma_1 = 1$, $\sigma_1 = 1–2R$ and $\sigma_1 = -1$ allows the calculation of I only from the orientation of the principal stress axes, the shape ratio R and the coefficient of friction μ (Vavryčuk (2014)):

$$I = \frac{\tau - \mu(\sigma_n - 1)}{\mu + \sqrt{1 + \mu^2}} \tag{3}$$

In this study, we assume a coefficient of friction of $\mu = 0.75$ (Byerlee, 1978; Sibson, 1983). Additionally, the direction of the expected fault slip represented by the rake λ, can be calculated (Aki & Richards, 1980; Allmendinger et al., 2012). λ depicts the in-plane angle of the shear traction with respect to the strike direction. The sign convention of Aki and Richards (1980) is used here, where negative values indicate components of normal slip and positive values denote components of reverse slip (Figure 1k). With the fault stress analysis module, both fault instabilities and kinematics can be estimated for each earthquake event.

3. Benchmarking With Synthetic Data

In order to assess the accuracy of the presented approach, we performed a test with a synthetic data set. For this data set, five rectangular planes were generated with the software Move™ (Petex v2019.1). Along these planes, a total of 605 points that represent synthetic hypocenter locations were sampled on a regular 100 m grid. To include the location uncertainties, the points were shifted randomly between 0–10 m horizontally and 0–100 m vertically. These values are in the range of formal relative errors estimated for local-scale, high-precision double-difference relocations with dense networks (e.g., Diehl et al., 2017; Simon et al., 2021), similar to the earthquake catalogs used in our study. Such formal relative errors can be theoretically achieved with differential-time measurements resolved at scales of a few miliseconds, which is possible by waveform CC, using seismograms resampled with a sample interval of 1 ms (e.g., Poupinet et al., 1984). A random M_L magnitude between zero and three was assigned to each hypocenter. In addition, 60 random events were inserted to reflect a background noise level of 10%. The synthetic hypocenter data set shown in Figure 2a was then analyzed with the fault network and automatic classification modules using parameters $n_{MC} = 1000$, $r_{NN} = 400$ m, an infinite search time dt_{NN}, and an expected number of clusters of $n_{clust} = 5$.

The resulting 3D fault network is shown in Figure 2b, where each earthquake is represented by a fault orientation stemming from the PCA and the respective circular fault size determined by the magnitude-area scaling. The orientation reliabilities κ are expressed by the opacity of the fault planes. The colors reflect the association to the different faults according to the automatic classification, and the corresponding results show that all 5 initial fault planes were successfully identified (Figures 2b and 2c). For the isolated fault A, the orientation reliability κ is higher in the center of the fault and decreases toward the edge. For the more complex fault geometries B to E, κ reveals several limitations of the method. Lower κ values are observed at the bends between faults C and D, respectively C and E (Figure 2b), which can be attributed to the non-planar arrangement of the hypocenters. κ is also reduced near the intersection of faults B and E, while for the intersecting part itself no fault planes could be calculated at all (Figure 2b). In the stereographic projection in Figure 2c, clear single-pole maxima are obtained in the case of the isolated fault plane (A) or intersecting fault planes with different dip directions and dip angles (B, E). For faults with similar dip angles and only variable dip directions (B, C, D), poles are smeared and cannot be reliably distinguished. These findings suggest that more complex natural fault structures, such as horsetails or duplexes, might not be well resolved with our approach. In general, a sufficient number of earthquakes along a fault and high-precision locations of the hypocenters are required to reliably image such second-order fault structures. Nevertheless, the benchmarking test with the synthetic data set demonstrates that our method is capable of imaging the overall fault-network geometry from high-quality hypocenter relocations. For natural earthquake sequences, the validation module should be used to assess the reliability of the reconstructed fault-network geometry by comparing the obtained fault orientations with the independent focal mechanisms (see Section 4.2).

4. Application to Natural Microearthquake Sequences

4.1. Geological Setting and Recent Seismicity

To demonstrate the effectiveness of the proposed approach for natural microearthquake sequences, we applied the algorithm to two sequences in the Southwestern Swiss Alps. The earthquakes in this area occur mainly

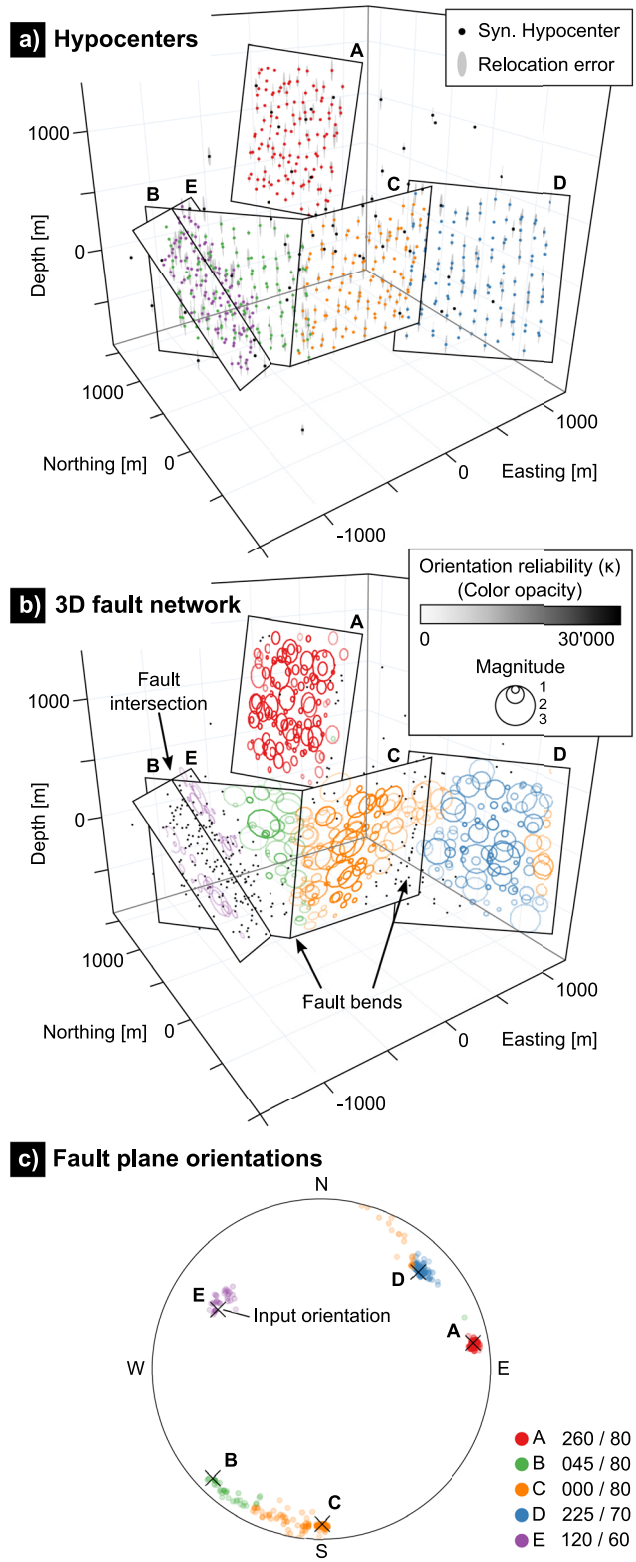

Figure 2. Results of the benchmarking with the synthetic data set. (a) Input model with randomized synthetic hypocenters and associated location errors that were sampled along five fault planes with 10% background noise. (b) 3D fault-network model recovered with the proposed method. The colors refer to five automatically detected and classified fault systems (colored). Each earthquake is represented by a circular fault rupture plane, where the opacity of the color reflects the orientation reliability. Gray points are events without a calculated fault plane. (c) Stereographic comparison of input and calculated fault-plane orientations (poles to planes, lower hemisphere, fault orientations: dip direction/dip angle in degrees).

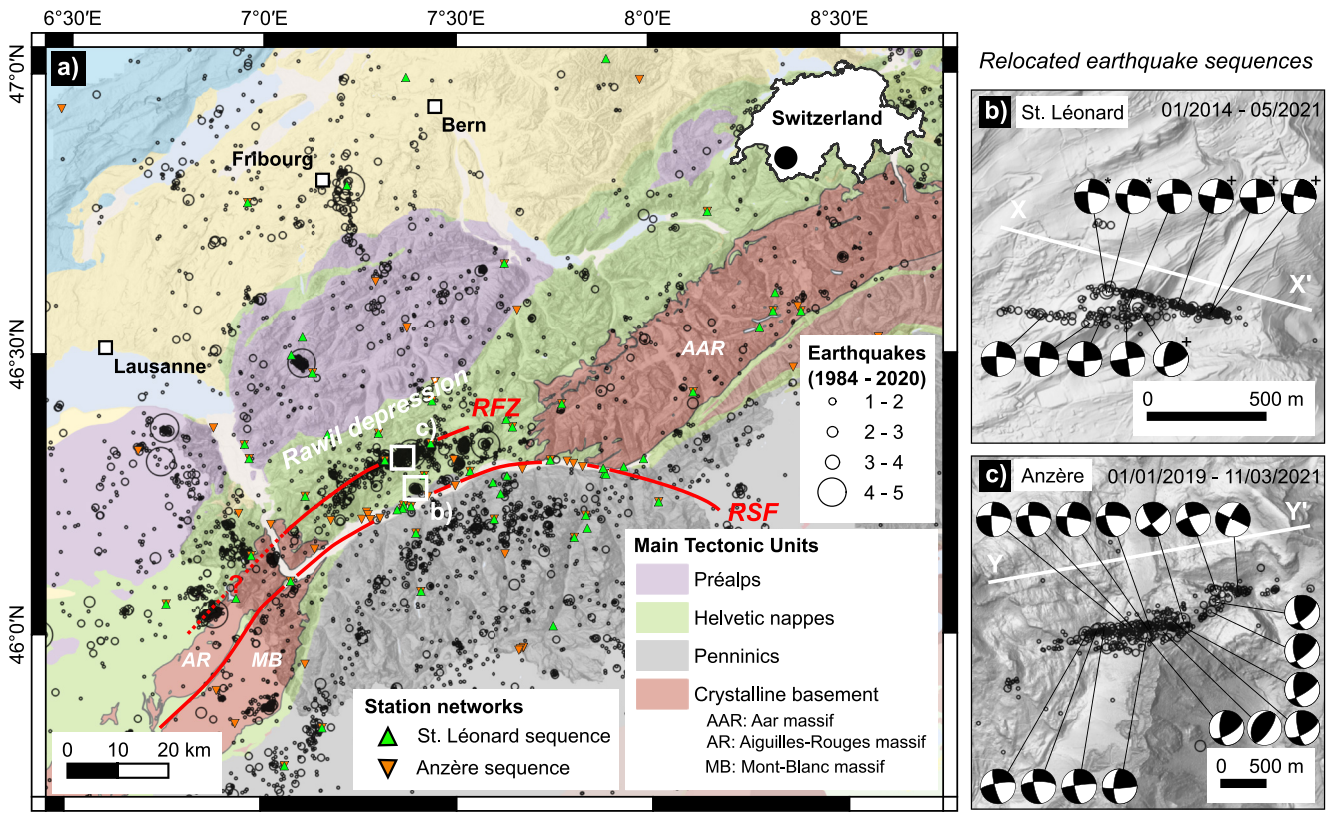

Figure 3. Map of the study area, showing (a) the main tectonic units and the absolutely relocated earthquake catalog from Diehl, Kissling et al. (2021). The Rhone-Simplon Fault System (RSF) and the Rawil Fault Zone (RFZ) are indicated with red lines. The relatively relocated hypocenters and focal mechanisms (see Figures S1 and S2 in Supporting Information S1 for details) of the (b) St. Léonard and (c) Anzère earthquake sequences derived in this study are shown in the right panels. The profile traces in (b) and (c) refer to the cross-sections in Figure 7. A complete list of the used stations for the relative earthquake relocations can be found in the data repository (Truttmann et al., 2023a). References of previously published focal mechanisms as shown in (b): + Diehl et al. (2018),* Diehl, Clinton, et al. (2021). Tectonic map after Swisstopo (2005).

in a NE-SW-directed, elongated cluster ranging from 0 to 8 km depth (e.g., Diehl, Kissling, et al., 2021; Lee et al., 2023; Figure 3a). This cluster lies in the Rawil depression, a saddle-like structure formed by the crystalline basement units (Burkhard, 1988; Cardello et al., 2016; Cardello & Mancktelow, 2015; Dietrich, 1989; Dietrich & Casey, 1989; Ramsay, 1981, 1989), which are dissected by steeply dipping and approximately NE-SW striking shear zones (e.g., Baumberger et al., 2022; Egli et al., 2017; Egli & Mancktelow, 2013; Herwegh et al., 2020). These units are exposed as the Aar massif in the NE and the Aiguilles Rouges and Mont Blanc massifs in the SW and are overlain by the folded limestone units of the Helvetic nappes in the Rawil depression. The suggested depth of the basement-cover contact below this depression is about 3–6 km (Burkhard, 1988; Levato et al., 1994; Pfiffner et al., 1997; Steck et al., 1997). A seismically active, regional-scale fault, called the Rawil Fault Zone (RFZ), is proposed below the Rawil depression (Burkhard, 1988; Cardello & Mancktelow, 2015; Lee et al., 2023; Maurer et al., 1997). To the South, the Rawil depression is bounded by the rather conceptual Rhone-Simplon Fault System (RSF) (e.g., Campani et al., 2010, 2014; Egli & Mancktelow, 2013; Mancktelow, 1985). Both of these regional fault systems have been attributed to the occurrence of earthquakes in the past (e.g., Diehl et al., 2018; Diehl, Clinton, et al., 2021; Lee et al., 2023).

In this study, we analyze two microearthquake sequences that occurred within, respectively close to the main seismic cluster and were recorded by a dense network of seismological stations (approximate interstation-distance <10 km; Diehl, Kissling, et al., 2021). Within 25 km distance, about 16–26 stations recorded P and S phases of these sequences. Figure 3b shows a map view of the relatively relocated St. Léonard sequence, which has already been partly analyzed by Diehl et al. (2018). The recompiled and updated sequence consists of 314 earthquakes that occurred at depths of about 7 ± 1 km (e.g., Lee et al., 2023) and includes events from January 2014 to May 2021. After a swarm-like occurrence of events between 2015 and 2018, three distinctive peaks of activity can be

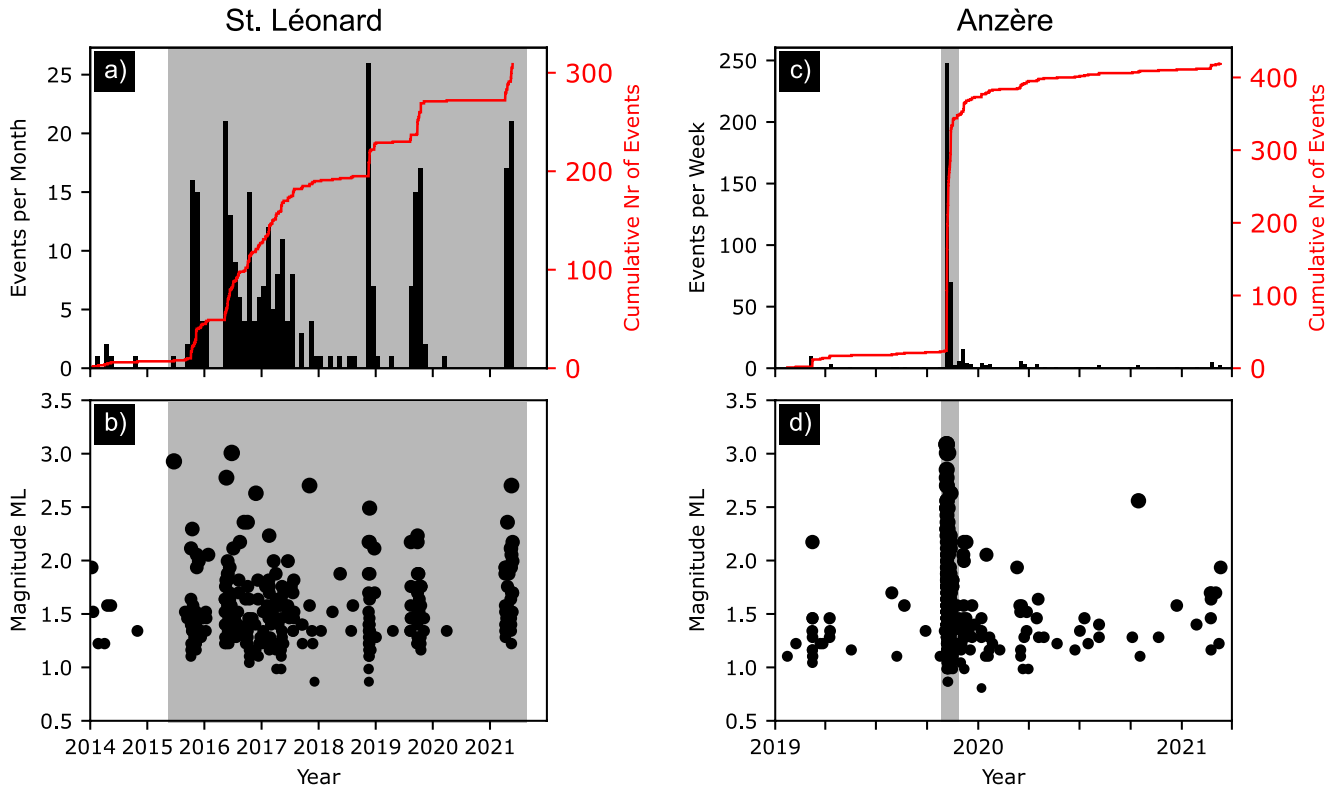

Figure 4. Temporal evolution of the earthquake sequences analyzed in this study. (a) Histogram of the monthly events and (b) M_L magnitudes of the St. Léonard sequence. (c) Histogram of the weekly events and (d) M_L magnitudes of the Anzère sequence. The gray areas mark the time period analyzed in Figure 7.

recognized in fall 2019 and 2020, as well as in spring 2021 (Figure 4a). The largest observed magnitude of the St. Léonard sequence corresponds to $M_L = 3.2$, whereas no isolated mainshock can be identified (Figure 4b). Six focal mechanisms from Diehl et al. (2018) and Diehl, Clinton, et al. (2021), as well as five additionally derived focal mechanisms are used for the St. Léonard case (see Figure S1 in Supporting Information S1 for details). As described in Section 2.1, we only considered uniquely constrained types of mechanisms (defined by a maximum angular difference of 30°), and the uncertainties, represented by the spread of possible solutions (gray lines in Figure S1 in Supporting Information S1), indicate that most of the mechanisms are well constrained. The Anzère sequence is shown in Figure 3c and preliminary results were reported in Diehl et al. (2021a). It consists of 420 relocated earthquakes recorded between January 2019 and March 2021. In contrast to the St. Léonard case, the Anzère sequence shows characteristics of a mainshock-aftershock sequence with an Omori-type aftershock decay (Figure 4c). Two $M_L = 3.3$ mainshocks were recorded on 5 November 2019, with the main activity within about 20 days thereafter at depths between 3 and 5 km (Figure 4d). In total, 17 reliable focal mechanisms have been considered for the analysis of the Anzère sequence (see Figure S2 in Supporting Information S1 for details). Using the same quality criteria as for the St. Léonard case, we consider the majority of these 17 mechanisms as well constrained and of high quality.

4.2. The St. Léonard Sequence

In order to image the seismically active fault systems, the 314 microearthquakes of the St. Léonard sequence were first relocated following the double-difference procedure outlined in Section 2.1. The initial number of quality-checked CC differential times used in the hypoDD inversion is high (190,030 differential times for P and 223,626 for S) and the final root-mean-square (RMS) residual of the CC data is 3 ms. A test with a subset of 107 events shows that the 3σ relative relocation errors derived from our resampling approach are several times larger than the formal uncertainties derived by the Singular Value Decomposition (SVD) solver of hypoDD (see Text S1 and Table S1 in Supporting Information S1 for details). The resampling approach yielded mean values for the 3σ relative relocation errors of ±15, ±21, and ±105 m in the x, y, and z directions for the complete set of events

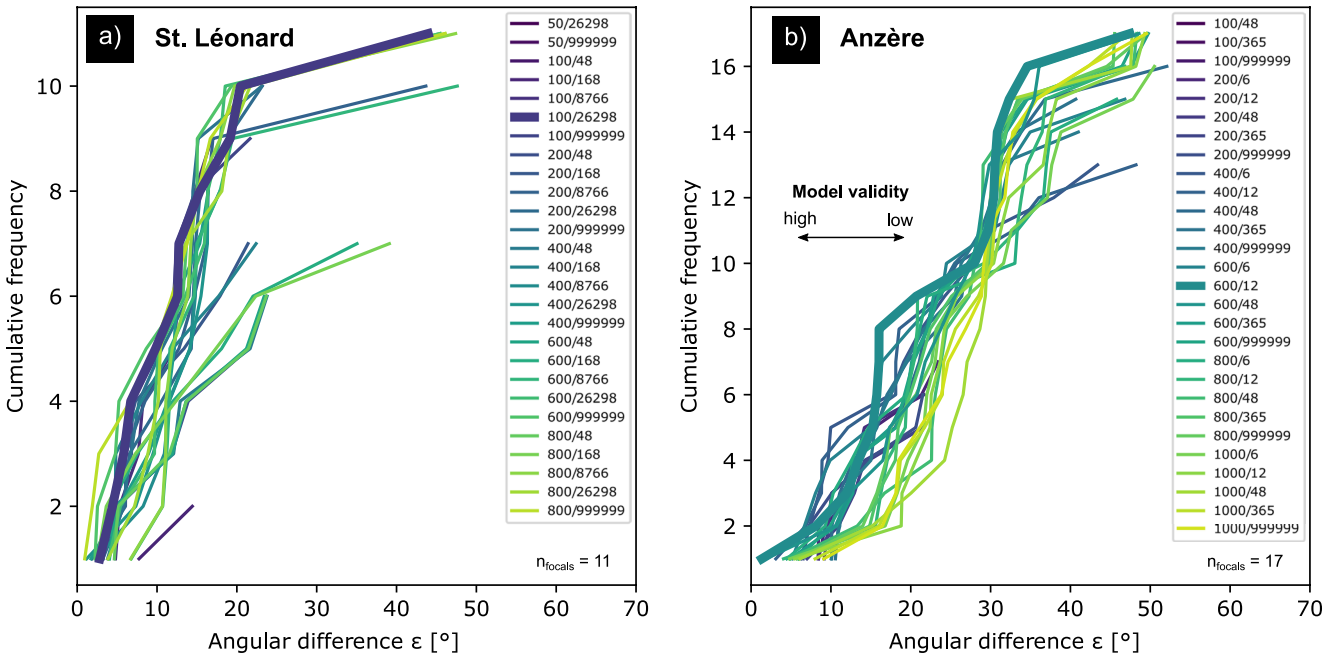

Figure 5. Cumulative frequency plots of ε_{min} to calibrate the input parameters r_{NN} and dt_{NN}. (a) Sensitivity analysis for the St. Léonard sequence. (b) Sensitivity analysis for the Anzère sequence. The model validation module was used to compare the calculated fault-plane orientation with the independently derived focal planes in order to determine optimal values for these parameters. r_{NN} is given in meters before the slash, dt_{NN} in hours after the slash.

(Figure S4 and Table S2 in Supporting Information S1). Considering the presumable fault length of microearthquakes on the order of ten to hundred meters (e.g., Bohnhoff et al., 2009), our 3σ relative errors derived from the resampling approach appear realistic (especially in comparison with the unrealistically small formal SVD errors) and in line with values reported in other studies (e.g., Bouchaala et al., 2013; Deichmann & Giardini, 2009; Simon et al., 2021; Trugman & Shearer, 2017; Valoroso et al., 2013; Waldhauser & Ellsworth, 2000). These relative uncertainties, however, represent formal errors, which do not consider effects related to possible small-scale, source-sided velocity variations (e.g., Diehl et al., 2017) as well as systematic errors of the 1D velocity model, possibly affecting the relative scaling of the cluster.

For formal relative errors on the order of few tens of meters, we found $n_{MC} = 1000$ to be sufficient to represent normally distributed Monte Carlo hypocenter datasets (Figure S3 in Supporting Information S1). To find the optimal values for the input parameters r_{NN} and dt_{NN}, as well as to ensure the validity of the recovered 3D fault network, the validation module as described in Section 2.2.2 was used to conduct a sensitivity analysis for the two parameters. For this, the cumulative frequency distributions of ε_{min} were plotted to analyze the influence of different r_{NN} and dt_{NN} on the model fit (Figure 5a). A perfect model would result in a full agreement between the fault-plane orientations derived by the algorithm and the independent focal mechanisms, which means that all values of ε_{min} would be zero and the curve would be vertical and equal to the *y*-axis. Following this concept, different combinations of r_{NN} and dt_{NN} were iteratively tested with resulting optimal values of $r_{NN} = 100$ m and $dt_{NN} = 26298$ hr (3 years) (Figure 5a). Using these parameters, a fault plane could be derived for ~75% of the events. Since the number of derived focal mechanisms is too small for a robust stress inversion (e.g., Martínez-Garzón et al., 2016), we used the well-accepted regional stress field of the Southwestern Swiss Alps derived by Kastrup et al. (2004). This stress field has principal stress axes of $\sigma_1 = 301/23$ (trend/plunge in degrees), respectively $\sigma_3 = 043/26$, and a shape ratio of $R = (\sigma_1–\sigma_2)/(\sigma_1–\sigma_3) = 0.35$ (Gephart & Forsyth, 1984), indicative for a transtensional regime. The regional stress field orientations are consistent with the principal stress axes suggested by the focal mechanisms. A value of $n_{clust} = 2$ was used for the automatic classification of the fault planes.

The resulting model reveals a system of two parallel, ESE-WNW striking main faults with a mean orientation of 192/89 (dip direction/dip angle in degrees). Both main faults have individual lengths of about 500 m, are laterally separated by ca. 200 m and have an overlap of 600–700 m (Figures 6a and 6b). The two vertical main faults are connected by an ENE-WSW striking fault (mean orientation 359/84, Figure 6c) that shows intersections

with both main faults A and B (Figure 6a). Inferring from this, we interpret this structure as a stepover fault. The vertical and along-strike extent of the entire active part of the fault system is approximately 1 km. A few hypocenters locate about 400 m north of the main fault structure, which might suggest the existence of a third ESE-WNW striking fault (Figure 6b). The orientation reliability, as indicated by the κ value, is high in the center of main fault A, while significantly lower at the bottom of the structure and within the stepover. This is consistent with the angular differences $\varepsilon_{\min}$, which indicate high values (and therefore higher uncertainties) at the bottom of main fault A (Figure S5a in Supporting Information S1). The relatively higher fault instability values between 0.8 and 1 for the main faults indicates that they are optimally oriented in the present-day stress field of the region, while the stepover has instability values between 0.5 and 0.8 and is thus less prone to reactivation (Figure 6d). The slip vectors shown in Figure 6e show the predicted kinematics for each event, which is mainly dextral strike-slip. Nonetheless, one focal mechanism within the stepover displays oblique thrusting, indicating a compressive regime. In summary, the hypocenter-based fault imaging approach discloses a system of optimally oriented, overlapping dextral strike-slip faults with a left-stepping contractional stepover.

In order to study the 3D spatiotemporal evolution, the events within the defined time window shown in Figure 4a were grouped into five time intervals from t_0 to t_4. A time interval was defined as a series of events that are both close in space and time, and separated to other time intervals by a period of reduced seismic activity. The first event of each interval is defined as the nucleation event. The spatiotemporal analysis was conducted in both 3D (Figure 7a) and in an along-strike profile (Figure 7b). Interval t_0 started with an isolated $M_L = 3.1$ earthquake on main fault A, that was followed by a small aftershock sequence. After about 5 months without any recorded seismicity, t_1 nucleated again on main fault A, followed by a migration of the seismicity toward the east and the west. Within the western branch of the migrating seismicity, an $M_L = 3.2$ event occurred at the intersection of the stepover and the main fault A. While seismicity migrated further westward, the migration velocity droped from about 0.27 m/hr along the main fault A to 0.03 m/hr within the stepover. All the events associated with this slower migrating branch also show significantly lower fault instability values. For about 2 years, earthquakes occurred along main fault A and the stepover in a swarm-like, diffuse manner, followed again by a quiescence period (i.e., no events above the M_c threshold) of almost 1 year. Interval t_2 nucleated again on the main fault A with east- and westward migrating seismicity, with the activity restricted to about 6 weeks, followed again by seismic quiescence for almost 1 year. The nucleation event of t_3 located close to the intersection of main fault B and the stepover, and was followed by a sequence of events within the stepover that migrated backwards toward main fault A. All these earthquakes occurred in a shallower part of the stepover than during t_1, documenting the propagation of the seismicity around the previously ruptured patches of the stepover. The 3 months of activity during t_3 were followed by seismic quiescence of about 1.5 years. Subsequently, t_4 marks the reactivation of main fault B, with mainly eastward migrating seismic activity during 7 weeks. Overall, the 3D spatiotemporal analysis of the St. Léonard sequence documents the cyclic reactivation of a contractional stepover fault system, and a drop in migration velocity of a factor of 10 within the stepover fault.

4.3. The Anzère Sequence

The 420 microearthquakes associated with the Anzère sequence were relocated following the double-difference procedure described in Section 2.1. While the total number of microearthquakes is higher than in the St. Léonard case, the initial number of quality-checked CC differential times is slightly smaller (151,515 differential times for P and 129,575 for S). The final RMS residual of the CC data is 2 ms. The relative relocation errors were assessed in a similar way as described for the St. Léonard case (see Text S1 and Table S3 in Supporting Information S1 for details). The resampling approach yielded mean values for the 3σ relative relocation errors of $\pm$54, $\pm$51, and $\pm$105 m in the x, y, and z directions for the complete set of events of the Anzère sequence (Figure S4 and Table S4 in Supporting Information S1). As discussed for the St. Léonard sequence in Section 4.2, we consider these 3σ relative relocation errors to be realistic estimates. The larger horizontal uncertainties in the Anzère case might be related to the relatively fewer CC differential times compared to the St. Léonard case. Since the formal errors are in the same range as for the St. Léonard sequence, a value of 1,000 was selected for parameter n_{MC}. The sensitivity analysis resulted in optimal input parameters of $r_{NN} = 600$ m and $dt_{NN} = 12$ hr, which provides a good balance between the model resolution and the number of represented focal mechanisms (Figure 5b). We further used the above-mentioned stress field parameters of Kastrup et al. (2004), and a value of $n_{clust} = 2$. Using these input parameters, a fault plane was derived for ~60% of the events.

The resulting 3D fault-network model reveals a system of two E-W striking, subvertical main faults with a mean orientation of 176/82 (dip direction/dip angle in degrees) and a lateral separation of about 500 m (Figures 8a

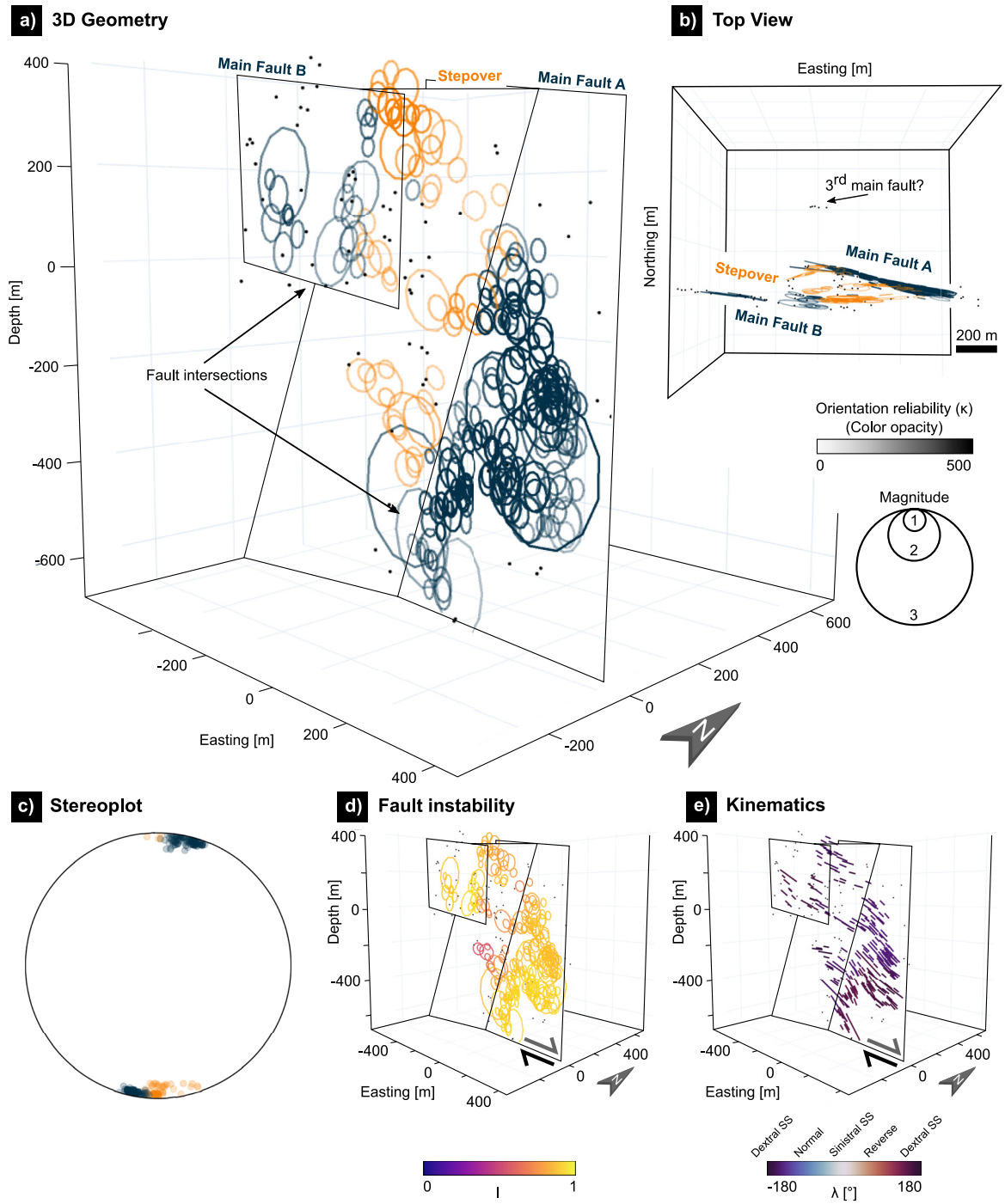

Figure 6. 3D fault-network model derived for the St. Léonard sequence with (a) and (b) showing the stepover fault system colored according to the automatic fault plane classification, (c) a stereographic projection of the fault planes (poles to planes, lower hemisphere), (d) the fault instability I (dimensionless) and (e) the kinematics defined by the rake angle λ (SS: strike slip). Axes are given in local coordinates, with the origin located at 46.264°N, 7.394°E and a depth of 6.7 km. The black dots indicate events without a calculated fault plane. Four outlier events far away from the main sequence are shown in the interactive version of this figure only (see Supporting Information S2).

and 8b). These parallel main faults have lengths of about 1.5 km (main fault A), respectively 0.5 km (main fault B) and are interconnected by an oblique, shallower dipping fault with a mean orientation of 163/78 (Figures 8a–8c). Due to the intersection with main fault B, we interpret this structure as a stepover (Figures 8a and 8b). In contrary to the St. Léonard sequence, the stepover is underlapping, with an along-strike separation of almost 1 km. The

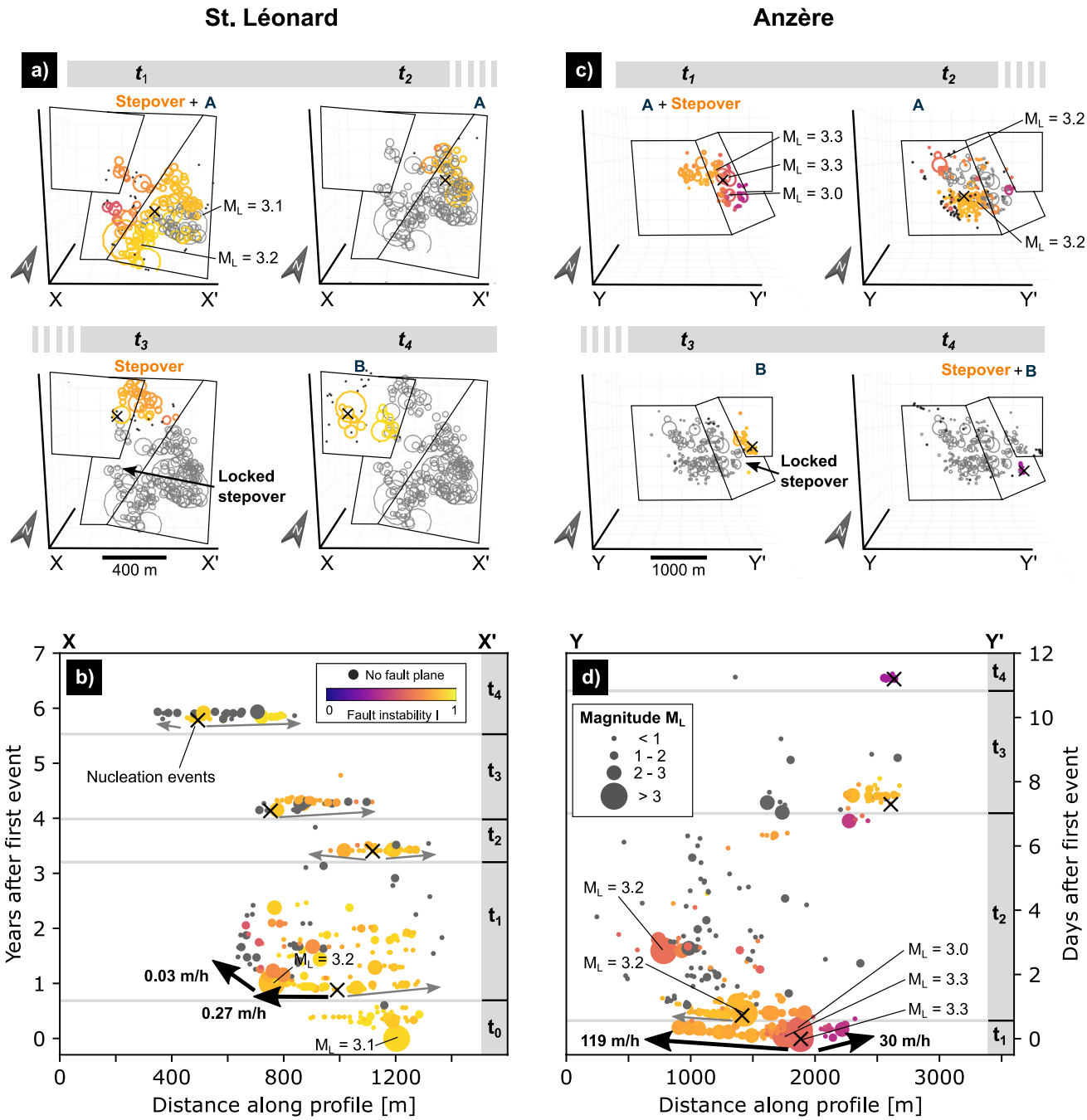

Figure 7. Spatiotemporal analysis of the two relocated earthquake sequences presented in 3D view (a and c) and as along-strike projection (b and d; profile traces shown in Figures 3b and 3c). The colors refer to the values of the fault instability parameter *I*, which is lower within the stepovers. Gray fault planes in (a) and (c) show all events which occurred before the respective time interval. Arrows in (b) and (d) indicate the migration direction and velocity of the seismicity.

total length of the active fault network is about 3 km, with a vertical extent of about 1.5 km. The high κ values along main fault A are in disagreement with the oblique reverse focal mechanisms, indicated by large values of ε_{min} (Figure S5b in Supporting Information S1). This shows that our model is not resolving the full structural complexity in this part. For both main faults, high fault instability values between 0.8 and 0.9 were found, while lower values between 0.3 and 0.8 were obtained within the stepover (Figure 8d). The slip vectors demonstrate predominant dextral strike-slip motion along both the main faults and the stepover, with a few indications of

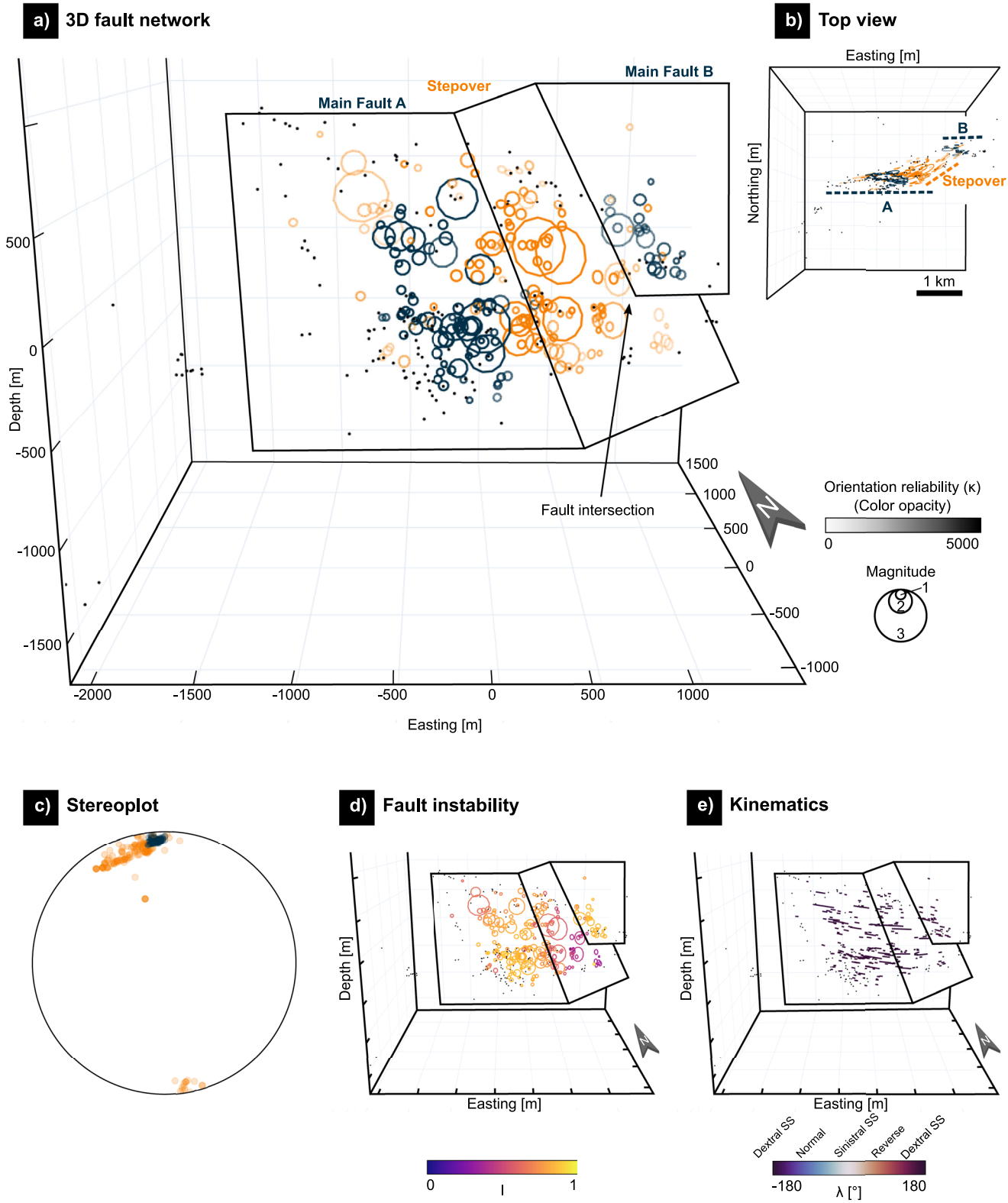

Figure 8. 3D fault-network model derived for the Anzère sequence with (a) and (b) showing the stepover fault systems colored according to the automatic fault plane classification, (c) a stereographic projection of the fault planes (poles to planes, lower hemisphere), (d) the fault instability I (dimensionless) and (e) the kinematics defined by the rake angle λ (SS: strike slip). Axes are given in local coordinates, with the origin located at 46.322°N, 7.355°E and a depth of 4.3 km. Five outlier events far away from the main sequence are shown in the interactive version of this figure only (see Supporting Information S2).

reverse movements exclusively within the stepover (Figure 8e). The modeled strike-slip movements within the stepover at least partly contradict the reverse-type focal mechanisms, indicating a compressional regime. Similar to the St. Léonard sequence, we image a system of subvertical underlapping dextral strike-slip faults with a left-stepping contractional stepover.

The 3D spatiotemporal analysis is restricted to the main activity during the 12 days after the mainshocks and is grouped into four separate time intervals (Figures 4c, 7c and 7d). Interval t_1 was initiated by an $M_L = 3.3$ mainshock that nucleated in-between main fault A and the stepover, 3 hr later followed by another $M_L = 3.3$ event within 130 m distance. Seismicity migrated both toward the west along main fault A and toward the east along the stepover. The migration velocity within the stepover of 30 m/hr was significantly lower than compared to the 119 m/hr within main fault A, coinciding with the reduced values of fault instability within the stepover. Another event with $M_L = 3.0$ occurred about 350 m away from to the first mainshock. After about 9 hr of seismic activity, t_2 nucleated on main fault A. The seismicity propagated mainly toward the west, with a first $M_L = 3.2$ event occurring close to the nucleation event, for which a reverse focal mechanism was derived (Figure S2i in Supporting Information S1). A second $M_L = 3.2$ earthquake occurred in a later stage of t_2 at a shallower part of main fault A, which is followed by few aftershocks along both main fault A and the stepover. Interval t_3 then marks the reactivation of main fault B. After almost 4 days of quiescence, t_4 reactivates another small part of the stepover. 20 days later, a small cluster of seismic activity could be observed on main fault B, imaging the lateral extent of this fault. In summary, these observations document the nucleation of two $M_L = 3.3$ mainshocks in close association with the contractional stepover and the consecutive seismogenic reactivation of the contractional stepover, again revealing significantly reduced migration velocities within the contractional stepover fault.

5. Discussion

5.1. Performance of the Algorithm

In this study, we have presented a new method to image the 3D geometries of active faults based on relocated hypocenters using nearest-neighbor learning and PCA, combined with a Monte Carlo-based approach to account for hypocenter relocation uncertainties. Compared to previous approaches, our method goes beyond the representation of faults as simple planar structures, but resolves geometrical complexities more accurately (e.g., Ouillon et al., 2008; Petersen et al., 2021; Wang et al., 2013). Since we treat each earthquake individually, and separate them both in space and time, our method is able to resolve small-scale structures which would not be resolved by fitting a single plane. As shown for the Anzère sequence, not all structural complexities are, however, appropriately resolved by the model. The spatial distribution of $\varepsilon_{\min}$ can be used to reveal such unmapped geometrical complexities (see Figure S5 in Supporting Information S1). Similar to Deichmann et al. (2014), we include the earthquake magnitude to approximate the rupture areas of individual events, which in contrast to other approaches images the areas of the fault network which actually ruptured (Kamer et al., 2020; Ouillon et al., 2008; Ouillon & Sornette, 2011). In addition, our method allows constraining variations in fault instabilities and kinematics within the reactivated fault networks. As shown in the supplementary material (Text S2 and Figures S6 and S7 in Supporting Information S1), the algorithm is able to recover fault-network geometries for other high-quality, relatively relocated microearthquake catalogs as well, demonstrating its general applicability.

Most published methods are limited by the necessity to pre-define the number of faults (Ouillon et al., 2008; Wang et al., 2013) or by the fact that the outcome depends on a large number of ad-hoc input parameters (Kamer et al., 2020; Meyer et al., 2019; Ouillon & Sornette, 2011). In contrast, our method uses a minimum number of simple, self-explanatory, and physically meaningful input parameters. The definition of the parameters r_{NN} and dt_{NN} is the most critical step in applying the method. Similar to Wang et al. (2013), we propose an approach that uses the independently derived focal mechanisms (i.e., the cumulative distribution of $\varepsilon_{\min}$) to calibrate these parameters. The uncertainties of the focal mechanisms are currently not reflected in our models, which might be included in future work. However, the majority of the focal mechanisms are well constrained, so we do not expect a significant impact on the parameter calibration. Since the parameter r_{NN} constrains the resolution at which planes are discriminated, an innapropriately large value might result in oversimplified models, while too small values lead to overfitted solutions or unconstrained plane fits. A first-order upper limit of r_{NN} is the rupture radius of the largest earthquake in the analyzed sequence, since a significantly greater value of r_{NN} would lead to spurious spatial correlations. The parameter dt_{NN} can be useful to resolve nearby faults that were seismically active at different times. For both r_{NN} and dt_{NN}, a compromise between the model resolution and the model

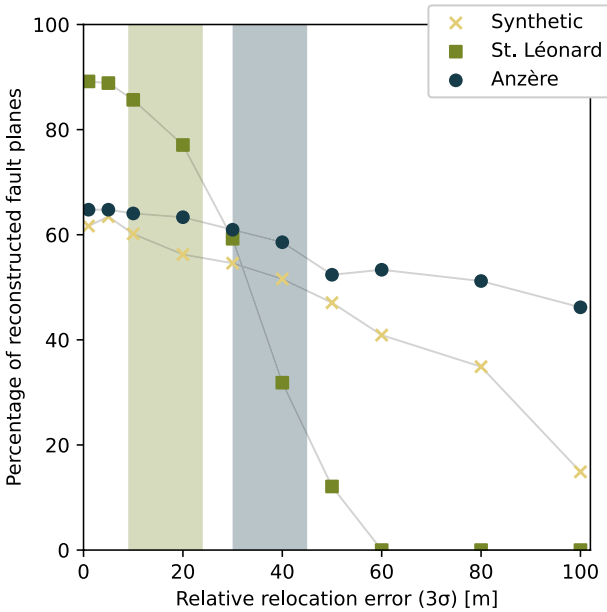

Figure 9. The algorithm performance, measured by the percentage of reconstructed fault planes, as a function of the horizontal relative relocation errors (3σ). The vertical errors are defined to be five times larger than the horizontal errors shown in the figure.

complexity has to be found. We emphasize that a proper calibration of the input parameters with independent constraints is a requirement to successfully apply our method on other microearthquake sequences. Since the exact parameters depend on the quality of the data set, which limits the final resolution, there is no generally applicable rule for the optimal set of parameters. The presented input parameter calibration using constraints from the focal mechanisms provides a guideline of how this could be achieved (see chapter 4.2 and Figure 5). Additionally, the obtained 3D fault networks should always be critically assessed and verified with geological considerations and the regional tectonic context.

The main requirements to apply our method to natural sequences are (a) high-precision hypocenter relocations with realistic formal uncertainty estimates and (b) a sufficient number of microearthquakes along the fault system. However, there also exist some limitations. The limited spatial resolution of the hypocenter datasets poses a challenge to our method, as it prevents us from accurately resolving fault structures at and below the scale of the formal relocation uncertainties. Additionally, larger relocation uncertainties can obscure the actual hypocenter distribution. To obtain more quantitative information on the required formal uncertainties, we analyzed the model performance for different relocation errors. The results of this analysis, shown in Figure 9, indicate that the 3σ horizontal relocation errors should not be significantly larger than 30–40 m for datasets similar to the ones used in this study (further details are available in Text S3 and Figure S8 in Supporting Information S1). However, this threshold is not generally applicable but only gives a first-order estimate, since it is obvious that the Anzère sequence is much less sensitive to the relocation errors than the St. Léonard data set, which is most likely caused by differences in the spatial arrangement of the hypocenters. The necessity to rely on a considerable number of earthquakes further requires a frequent seismic activity, long-term monitoring or enhanced earthquake catalogs. The number of required earthquakes depends on the targeted model resolution and the extent of the fault systems, but the method should certainly not be applied on hypocenter catalogs with less than several hundreds of events. Major advances in microearthquake detection and relocation procedures, such as template matching detection or machine learning approaches and combinations of such methods (e.g., Mousavi et al., 2020; Shi et al., 2022; Simon et al., 2021; Zhu & Beroza, 2019), will provide new datasets that fulfill these requirements or enhance existing ones in future applications. Finally, it should be noted that our approach resolves only faults which rupture seismically. Hence, information on aseismic deformation such as elastic loading or aseismic creep is lacking. Despite these limitations, the presented method has great potential for future seismotectonic studies of active fault zones.

5.2. Active Faults Along the Rhone-Simplon Fault System

The application of our method to the double-difference relocated St. Léonard and Anzère sequences allows for imaging the detailed 3D geometries of active faults that are part of the previously proposed, ENE-WSW striking RSF and RFZ (Deichmann et al., 2012; Diehl et al., 2018; Diehl, Clinton, et al., 2021; Lee et al., 2023; Maurer et al., 1997). The presence of stepover faults in the respective fault systems has been postulated by some of these authors before, but the detailed fault structures were not resolved. Contractional stepovers are common features in strike-slip fault systems with different Riedel-type structures, as shown in Figure 10 (Dooley & Schreurs, 2012; Pennacchioni & Mancktelow, 2013; Swanson, 1988, 2005; Sylvester, 1988; Woodcock & Fischer, 1986). In both analyzed sequences, the E-W to ESE-WNW striking main faults can be described as Y-shears and represent the principal slip zones, while the stepover faults have orientations similar to P shears (Kim et al., 2004; Peacock & Sanderson, 1995; Pennacchioni & Mancktelow, 2013). The overlapping stepover of the St. Léonard sequence exhibits a length-to-width ratio of around 3–4, which is comparable to previously observed values (e.g., Manighetti et al., 2021). The smaller percentage of recovered fault planes for the Anzère sequence (~60%) compared to the St. Léonard sequence (~75%) can be explained by the more distributed hypocenters, potentially resulting from a larger amount of off-fault seismicity or a less developed high-strain slip zone (Ross et al., 2017). In light of such interpretations it is however important to remember that our method only resolves the seismically active part of the fault networks, so fault patches without any

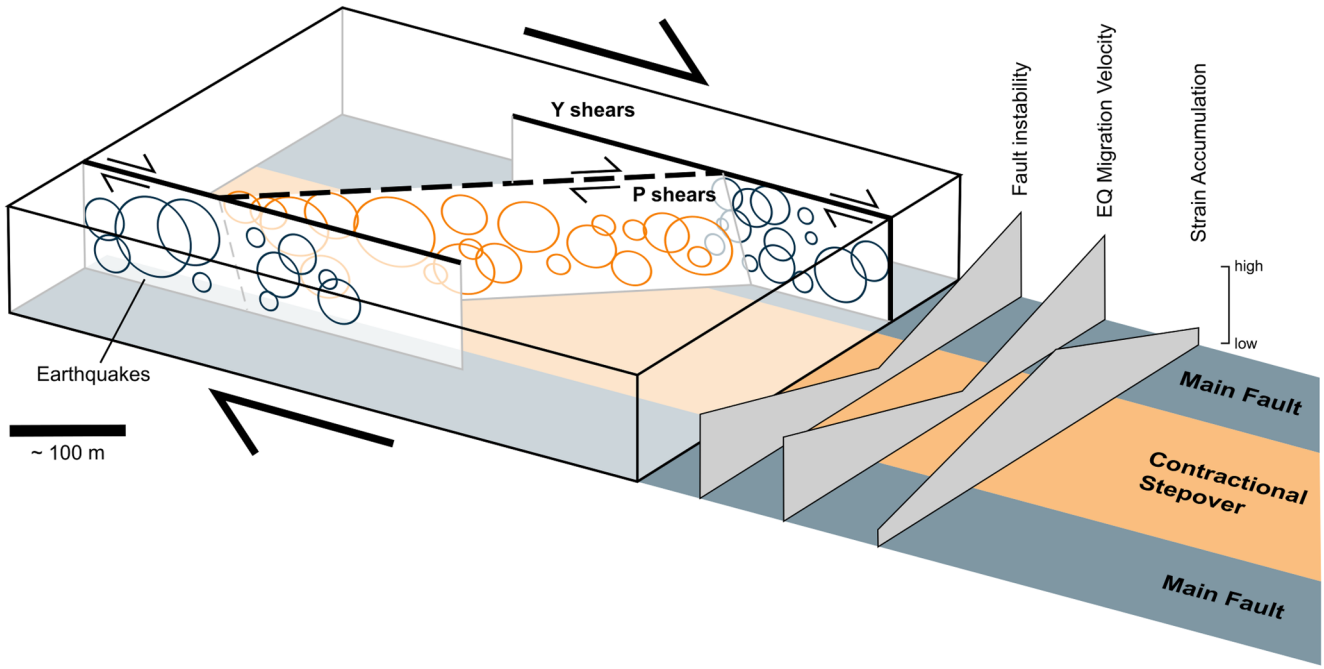

Figure 10. Schematic illustration of the contractional stepovers and the reactivated Y and P shears imaged for the two earthquake sequences analyzed in this study. Suggested properties for the different parts of the faults are shown to the right, generally matching the observations for both sequences.

release of seismic energy might not be discovered, and the actual extent of the pre-existing faults would consequently be underestimated. As an alternative hypothesis, the stepovers might be interpreted as a system of en-echelon faults. However, due to the striking correlation between the reconstructed fault planes and the respective nodal planes of the focal mechanisms within the stepovers, we consider this scenario less likely and favor the first-mentioned hypothesis.

Strike-slip fault systems similar in terms of orientations and dimensions have also been reported from field observations in the Rawil depression (Cardello & Mancktelow, 2015). In combination with the observation of the regional fault systems and earthquake clusters shown in Figure 3a (Diehl, Clinton, et al., 2021; Lee et al., 2023), this suggests that the imaged, E-W to NE-SW striking faults are small-scale expressions of the more regional fault systems. In the case of the Anzère sequence, the imaged structure can be clearly linked to the RFZ, since the studied earthquake sequence lies in close vicinity of this regional fault system (Figure 3a). The active RFZ was first identified by Maurer et al. (1997) and confirmed by recent findings of Lee et al. (2023), who showed that the ENE-WSE trending cluster of seismicity cuts through both the Helvetic nappes and the crystalline basement. With depths around 4–6 km, the imaged Anzère fault system is supposedly located in close proximity to the basement-cover contact. Due to their more southern location, the active faults of the St. Léonard sequence are likely not part of the main RFZ (Figure 3a). Located at a depth of around 6–7 km, these faults most likely lie within the crystalline basement units. Their regional tectonic context is however more difficult to assess, but we speculate that they either represent the diffuse, deep-rooted eastern termination of the RFZ (Lee et al., 2023), or belong to a northern branch of the RSF.

The newly imaged stepovers show that our algorithm, applied on high-quality relatively relocated microearthquake sequences, has great potential to gain detailed insights into the 3D architectures of seismogenic faults at depth. This is of relevance, since the 3D fault architecture plays an important role in the nucleation, propagation and termination of earthquakes (e.g., Barka & Kadinsky-Cade, 1988; Finzi & Langer, 2012a, 2012b; Ross et al., 2020; Segall & Pollard, 1980; Wibberley et al., 2008). More detailed information about abundance, geometries, and properties of such active fault systems at depth is required to improve the hazard assessment of known active faults. To achieve this goal, we argue that seismological constraints should be complemented with refined geological surface observations.

5.3. Seismogenic Reactivation of Stepovers

The two investigated microearthquake sequences show striking similarities in terms of the spatiotemporal fault reactivation. In both cases, the migration velocities within the stepovers are reduced by one order of magnitude

compared to the main faults. Decreased migration velocities within stepovers have been previously observed, for example, by Harris & Day (1993). The positive correlation between the migration velocities and the fault instability values in our analysis implies that the main faults are optimally oriented and thus more prone to reactivation than the stepovers (Figures 6, 8 and 10), which is in agreement with the observation that most nucleation points are located at sites of enhanced fault instabilities (Figure 7). These findings also align well with the observations of De Barros et al. (2021), who related reduced migration velocities to less critically stressed faults. Despite being less optimally oriented in the regional stress field, reduced migration velocities within the stepover could also be explained by other factors. Slip along the main faults, for example, might increase the compressive stresses within the stepover, which enhances its frictional resistance and thus reduce the migration velocities (Oglesby, 2005; Sibson, 1986). Additionally, a higher degree of fracturing within the contractional stepovers could provide a weak barrier that slows down migrating earthquakes (Segall & Pollard, 1980; Sibson, 1986). The presence of overpressurized fluids within the stepovers could also contribute to such a weak barrier and lead to slower migration velocities (Sibson, 2014, 2020). Despite the spatiotemporal similarities, the different dynamics of the two analyzed microearthquake sequences imply contrasting mechanisms (Roland & McGuire, 2009; Vidale & Shearer, 2006). For the Anzère sequence, the estimated migration velocities of 30–119 m/hr are indicative for aseismic slip (Chen & Shearer, 2011; Lohman & McGuire, 2007; Roland & McGuire, 2009). In contrary, migration velocities of 0.03–0.27 m/hr for the St. Léonard case suggest fluid diffusion as the main driver (Chen & Shearer, 2011; Roland & McGuire, 2009). The dual migration pattern documented for the latter, with a slow overall migration and rapid seismic burst, could however also be related to an interaction of long-term fluid diffusion and aseismic slip events (Dublanchet & De Barros, 2021).

It is also interesting to note that the stepover faults are spatially reactivated only once during the investigated time period, while the same patches of the main faults are reactivated multiple times. We thus interpret these observations as temporal frictional locking of the more stable stepovers (Figures 7b and 7d) (e.g., Malservisi et al., 2003; Moreno et al., 2010; Qiu et al., 2016). Locked stepover faults are capable to accommodate internal strain and thus enable the transfer of stresses from one optimally oriented main fault to an adjacent one, which could explain the observed overall migration of the earthquakes from one strike-slip fault to the next one. Continuous strain accumulation within the contractional stepovers can also promote the nucleation of earthquakes (Barka & Kadinsky-Cade, 1988; Oglesby, 2005; Segall & Pollard, 1980; Wibberley et al., 2008). The observation of the mainshocks occurring in close association to the stepovers implies that these structures might have accumulated a significant amount of internal strain. Besides their influence on earthquake nucleation processes, stepover faults can also act as natural barriers and terminate earthquake ruptures (Elliott et al., 2015; Oglesby, 2005; Wibberley et al., 2008). However, significantly larger earthquake ruptures than investigated in this study might not be effectively stopped at such tightly spaced, low-angle stepovers (Elliott et al., 2015). This could ultimately lead to a cascade of ruptures across several optimally oriented faults (e.g., Finzi & Langer, 2012a, 2012b; Manighetti et al., 2007).

In summary, the well-documented earthquake migration patterns across the stepover faults with variations in fault instabilities illustrate the strong influence of a faults' small-scale 3D architecture on seismogenic fault reactivation processes (Ross et al., 2020; Shelly, 2015). We thus emphasize that future analyses of microearthquake sequences should consider the potential influence of the 3D fault architecture on the observed spatiotemporal patterns, since this could significantly enhance our understanding of the mechanisms that trigger and drive earthquakes.

6. Conclusions

The developed method allows performing hypocenter-based 3D imaging of active faults, and has the potential to reveal previously undetected, small-scale 3D architectures of subsurface faults. Applied to high-quality, relatively relocated earthquake sequences, our method can thus significantly enhance the understanding of seismogenic fault reactivation processes. In summary, we can draw the following conclusions.

1. The presented hypocenter-based imaging approach allows for resolving the detailed 3D structures of active faults in the subsurface. The method enables the analysis of both fault instabilities and kinematics of the individual earthquakes, which gives new possibilities for the seismotectonic interpretation of seismic sequences and can thus contribute to next-generation seismic hazard assessment. Our approach could also be used for other applications on different scales, such as imaging large-scale active faults from regional earthquake catalogs, monitoring reactivated faults during hydraulic fracture stimulation, exploring natural sources of

hydrothermal fluids, or tracing artificially induced fractures in laboratory experiments. To further improve the performance of the algorithm, it could be applied to enhanced hypocenter catalogs obtained from a combination of template matching and DD relocation (e.g., Herrmann et al., 2019; Simon et al., 2021).

2. The application of the method to two natural earthquake sequences in the Southwestern Swiss Alps has revealed previously unknown fault structures. This demonstrates the method's potential to gain improved knowledge about the detailed 3D fault architecture of active faults in regions of distributed seismicity and faulting. To determine the overall regional significance of the identified fault systems and thus advance our understanding of the seismic hazard of the Southwestern Swiss Alps, investigations on a more regional scale are required. Possible next steps could involve a combination of field-based fault observations and application of the method to additional earthquake sequences.
3. The migration dynamics of the seismicity recorded in this study provide strong evidence for the significant impact of 3D fault architectures on earthquake rupture processes. Geometrical complexities, such as stepovers, also have direct implications for the physical fault zone characteristics, including the likelihood for reactivation, the accumulation of internal strain, and the hydrological properties. Therefore, we advocate for the inclusion of 3D fault architectures in future studies of seismogenic fault reactivation processes, wherever possible.

Conflict of Interest

The authors declare no conflicts of interest relevant to this study.

Data Availability Statement

The relocated hypocenter and focal mechanism datasets, the station networks, the hypoDD parameters, and the interactive 3D fault-network models are stored in the following repository under the CC BY 4.0 license: https://doi.org/10.5281/zenodo.7855039 (Truttmann et al., 2023a). The code used to perform the hypocenter-based 3D imaging of active faults is permanently stored in the following repository: https://doi.org/10.5281/zenodo.7854999 (Truttmann et al., 2023b). An actively develop version of the code is publicly available on Github under the GPL-3.0 license: https://github.com/sandrotruttmann/hypo_fault_imaging.

Acknowledgments
Comments by the editor Isabelle Manighetti, the anonymous associate editor, one anonymous reviewer, Luisa Valoroso, and Emily Warren-Smith helped to substantially improve an earlier version of the manuscript and are thankfully acknowledged. The authors thank Andrea Biedermann for her help with directional statistics. This work was funded by the Swiss Geophysical Commission and the Swiss Federal Office of Topography swisstopo, which is greatly acknowledged. Tobias Diehl acknowledges financial support from the Nationale Genossenschaft für die Lagerung radioaktiver Abfälle (Nagra). Petroleum Experts (Petex) kindly provided an academic license of the software Move™ to the Institute of Geological Sciences at the University of Bern. Open access funding provided by Universitat Bern.

References

Aki, K., & Richards, P. G. (1980). Quantitative seismology: Theory and methods.

Allmendinger, R. W., Cardozo, N., & Fisher, D. M. (2012). Structural geology algorithms: Vectors and tensors. *Structural Geology Algorithms*. https://doi.org/10.1017/CBO9780511920202

Banerjee, A., Dhillon, I. S., Ghosh, J., & Sra, S. (2005). Clustering on the unit hypersphere using von Mises-Fisher distributions. *Journal of Machine Learning Research*, *6*, 1345–1382. https://doi.org/10.1038/325754c0

Barka, A. A., & Kadinsky-Cade, K. (1988). Strike-slip fault geometry in Turkey and its influence on earthquake activity. *Tectonics*, *7*(3), 663–684. https://doi.org/10.1029/tc007i003p00663

Baumberger, R., Herwegh, M., Kissling, E., & Survey, S. G. (2022). Remote sensing and field data based structural 3D modelling (Haslital, Switzerland) in combination with uncertainty estimation and verification by underground data. In *Remote sensing and field data based structural 3D modelling* (pp. 159–197).

Bohnhoff, M., Dresen, G., Ellsworth, W. L., & Ito, H. (2009). Passive seismic monitoring of natural and induced earthquakes: Case studies, future directions and socio-economic relevance. In S. Cloetingh & J. Negendank (Eds.), *New frontiers in integrated Solid Earth Sciences. International year of Planet Earth*. Springer. https://doi.org/10.1007/978-90-481-2737-5_7

Borradaile, G. (2003). Statistics of Earth science data.

Bott, M. H. P. (1959). The mechanics of oblique slip faulting. *Geological Magazine*, *16*(2), 109–117. https://doi.org/10.1017/S0016756800059987

Bouchaala, F., Vavryčuk, V., & Fischer, T. (2013). Accuracy of the master-event and double-difference locations: Synthetic tests and application to seismicity in West Bohemia, Czech Republic. *Journal of Seismology*, *17*(3), 841–859. https://doi.org/10.1007/s10950-013-9357-4

Brunsvik, B., Morra, G., Cambiotti, G., Chiaraluce, L., Di Stefano, R., De Gori, P., & Yuen, D. A. (2021). Three-dimensional paganica fault morphology obtained from hypocenter clustering (L'Aquila 2009 seismic sequence, Central Italy). *Tectonophysics*, *804*(January), 228756. https://doi.org/10.1016/j.tecto.2021.228756

Burkhard, M. (1988). L'Helvétique de la bordure occidentale du massif de l'Aar (évolution tectonique et métamorphique). *Eclogae Geologicae Helvetiae*, *81*(1), 63–114.

Byerlee, J. (1978). Friction of rocks. *Pure and Applied Geophysics*, *116*(4–5), 615–626. https://doi.org/10.1007/BF00876528

Campani, M., Mancktelow, N., & Courrioux, G. (2014). The 3D interplay between folding and faulting in a syn-orogenic extensional system: The Simplon Fault Zone in the Central Alps (Switzerland and Italy). *Swiss Journal of Geosciences*, *107*(2–3), 251–271. https://doi.org/10.1007/s00015-014-0163-y

Campani, M., Mancktelow, N., Seward, D., Rolland, Y., Müller, W., & Guerra, I. (2010). Geochronological evidence for continuous exhumation through the ductile-brittle transition along a crustal-scale low-angle normal fault: Simplon Fault Zone, Central Alps. *Tectonics*, *29*(3). https://doi.org/10.1029/2009TC002582

Cardello, G. L., Almqvist, B. S. G., Hirt, A. M., & Mancktelow, N. S. (2016). Determining the timing of formation of the Rawil depression in the Helvetic Alps by palaeomagnetic and structural methods. *Geological Society - Special Publications*, *425*(1), 145–168. https://doi.org/10.1144/SP425.4

Cardello, G. L., & Mancktelow, N. S. (2015). Veining and post-nappe transtensional faulting in the SW Helvetic Alps (Switzerland). *Swiss Journal of Geosciences*, *108*(2–3), 379–400. https://doi.org/10.1007/s00015-015-0199-7

Chamberlain, C. J., Hopp, C. J., Boese, C. M., Warren-Smith, E., Chambers, D., Chu, S. X., et al. (2017). EQcorrscan: Repeating and near-repeating earthquake detection and analysis in Python. *Seismological Research Letters*, *89*(1), 173–181. https://doi.org/10.1785/0220170151

Chen, X., & Shearer, P. M. (2011). Comprehensive analysis of earthquake source spectra and swarms in the Salton Trough, California. *Journal of Geophysical Research*, *116*(B9), B09309. https://doi.org/10.1029/2011JB008263

Console, R., & Di Giovambattista, R. (1987). Local earthquake relative location by digital records. *Physics of the Earth and Planetary Interiors*, *47*(C), 43–49. https://doi.org/10.1016/0031-9201(87)90065-3

De Barros, L., Wynants-Morel, N., Cappa, F., & Danré, P. (2021). Migration of fluid-induced seismicity reveals the seismogenic state of faults. *Journal of Geophysical Research: Solid Earth*, *126*(11), 1–15. https://doi.org/10.1029/2021JB022767

Deichmann, N., Clinton, J., Husen, S., Edwards, B., Haslinger, F., Fäh, D., et al. (2012). Earthquakes in Switzerland and surrounding regions during 2011. *Swiss Journal of Geosciences*, *105*(3), 463–476. https://doi.org/10.1007/s00015-012-0116-2

Deichmann, N., & Giardini, D. (2009). Earthquakes induced by the stimulation of an enhanced geothermal system below Basel (Switzerland). *Seismological Research Letters*, *80*(5), 784–798. https://doi.org/10.1785/gssrl.80.5.784

Deichmann, N., Kraft, T., & Evans, K. F. (2014). Identification of faults activated during the stimulation of the Basel geothermal project from cluster analysis and focal mechanisms of the larger magnitude events. *Geothermics*, *52*, 84–97. https://doi.org/10.1016/j.geothermics.2014.04.001

Diehl, T., Clinton, J., Cauzzi, C., Kraft, T., Kästli, P., Deichmann, N., et al. (2021). Earthquakes in Switzerland and surrounding regions during 2017 and 2018. *Swiss Journal of Geosciences*, *114*(4), 4. https://doi.org/10.1186/s00015-020-00382-2

Diehl, T., Clinton, J., Deichmann, N., Cauzzi, C., Kästli, P., Kraft, T., et al. (2018). Earthquakes in Switzerland and surrounding regions during 2015 and 2016. *Swiss Journal of Geosciences*, *111*(1–2), 221–244. https://doi.org/10.1007/s00015-017-0295-y

Diehl, T., Kissling, E., Herwegh, M., & Schmid, S. M. (2021). Improving absolute hypocenter accuracy with 3-D Pg and Sg body-wave inversion procedures and application to earthquakes in the Central Alps region. *Journal of Geophysical Research: Solid Earth*, *126*(12), 1–26. https://doi.org/10.1029/2021jb022155

Diehl, T., Kraft, T., Kissling, E., & Wiemer, S. (2017). The induced earthquake sequence related to the St. Gallen deep geothermal project (Switzerland): Fault reactivation and fluid interactions imaged by microseismicity. *Journal of Geophysical Research: Solid Earth*, *122*(9), 7272–7290. https://doi.org/10.1002/2017JB014473

Dietrich, D. (1989). Fold-axis parallel extension in an arcuate fold- and thrust belt: The case of the Helvetic nappes. *Tectonophysics*, *170*(3–4), 183–212. https://doi.org/10.1016/0040-1951(89)90271-0

Dietrich, D., & Casey, M. (1989). A new tectonic model for the Helvetic nappes. *Geological Society - Special Publications*, *45*(45), 47–63. https://doi.org/10.1144/GSL.SP.1989.045.01.03

Dooley, T. P., & Schreurs, G. (2012). Analogue modelling of intraplate strike-slip tectonics: A review and new experimental results. *Tectonophysics*, *574–575*, 1–71. https://doi.org/10.1016/j.tecto.2012.05.030

Dublanchet, P., & De Barros, L. (2021). Dual seismic migration velocities in seismic swarms. *Geophysical Research Letters*, *47*(1), e2020GL090025. https://doi.org/10.1029/2020GL090025

Egli, D., & Mancktelow, N. S. (2013). The structural history of the Mont Blanc massif with regard to models for its recent exhumation. *Swiss Journal of Geosciences*, *106*(3), 469–489. https://doi.org/10.1007/s00015-013-0153-5

Egli, D., Mancktelow, N. S., & Spikings, R. (2017). Constraints from 40Ar/39Ar geochronology on the timing of alpine shear zones in the Mont Blanc-Aiguilles Rouges region of the European Alps. *Tectonics*, *36*(4), 730–748. https://doi.org/10.1002/2016TC004450

Elliott, A. J., Oskin, M. E., Liu-Zeng, J., & Shao, Y. (2015). Rupture termination at restraining bends: The last great earthquake on the Altyn Tagh fault. *Geophysical Research Letters*, *42*(7), 2164–2170. https://doi.org/10.1002/2015GL063107

Faulkner, D. R., Jackson, C. A. L., Lunn, R. J., Schlische, R. W., Shipton, Z. K., Wibberley, C. A. J., & Withjack, M. O. (2010). A review of recent developments concerning the structure, mechanics and fluid flow properties of fault zones. *Journal of Structural Geology*, *32*(11), 1557–1575. https://doi.org/10.1016/j.jsg.2010.06.009

Finzi, Y., & Langer, S. (2012a). Damage in step-overs may enable large cascading earthquakes. *Geophysical Research Letters*, *39*(16), 1–5. https://doi.org/10.1029/2012GL052436

Finzi, Y., & Langer, S. (2012b). Predicting rupture arrests, rupture jumps and cascading earthquakes. *Journal of Geophysical Research B: Solid Earth*, *117*(12), 1–11. https://doi.org/10.1029/2012JB009544

Frohlich, C., & Davis, S. D. (1990). Single-link cluster analysis as a method to evaluate spatial and temporal properties of earthquake catalogues. *Geophysical Journal International*, *100*(1), 19–32. https://doi.org/10.1111/j.1365-246X.1990.tb04564.x

Gephart, J. W., & Forsyth, D. W. (1984). An improved method for determining the regional stress tensor using earthquake focal mechanism data: Application to the San Fernando earthquake sequence. *Journal of Geophysical Research*, *89*(B11), 9305–9320. https://doi.org/10.1029/JB089iB11p09305

Gibbons, S. J., & Ringdal, F. (2006). The detection of low magnitude seismic events using array-based waveform correlation. *Geophysical Journal International*, *165*(1), 149–166. https://doi.org/10.1111/j.1365-246X.2006.02865.x

Goertz-Allmann, B. P., Edwards, B., Bethmann, F., Deichmann, N., Clinton, J., Fäh, D., & Giardini, D. (2011). A new empirical magnitude scaling relation for Switzerland. *Bulletin of the Seismological Society of America*, *101*(6), 3088–3095. https://doi.org/10.1785/0120100291

Hajnal, Z., Lucas, S., White, D., Lewry, J., Bezdan, S., Stauffer, M. R., & Thomas, M. D. (1996). Seismic reflection images of high-angle faults and linked detachments in the Trans-Hudson Orogen. *Tectonics*, *15*(2), 427–439. https://doi.org/10.1029/95TC02710

Hardebeck, J. L., & Shearer, P. M. (2002). A new method for determining first-motion focal mechanisms. *Bulletin of the Seismological Society of America*, *92*(6), 2264–2276. https://doi.org/10.1785/0120010200

Harris, R. A., & Day, S. M. (1993). Dynamics of fault interaction: Parallel strike-slip faults. *Journal of Geophysical Research*, *98*(B3), 4461–5572. https://doi.org/10.1029/92JB02272

Hauksson, E., & Shearer, P. (2005). Southern California hypocenter relocation with waveform cross-correlation, part 1: Results using the double-difference method. *Bulletin of the Seismological Society of America*, *95*(3), 896–903. https://doi.org/10.1785/0120040167

Herrmann, M., Kraft, T., Tormann, T., Scarabello, L., & Wiemer, S. (2019). A consistent high-resolution catalog of induced seismicity in basel based on matched filter detection and tailored post-processing. *Journal of Geophysical Research: Solid Earth*, *124*(8), 8449–8477. https://doi.org/10.1029/2019JB017468

Herwegh, M., Berger, A., Glotzbach, C., Wangenheim, C., Mock, S., Wehrens, P., et al. (2020). Late stages of continent-continent collision: Timing, kinematic evolution, and exhumation of the Northern rim (Aar Massif) of the Alps. *Earth-Science Reviews*, *200*(November 2019), 102959. https://doi.org/10.1016/j.earscirev.2019.102959

Husen, S., Kissling, E., Deichmann, N., Wiemer, S., Giardini, D., & Baer, M. (2003). Probabilistic earthquake location in complex three-dimensional velocity models: Application to Switzerland. *Journal of Geophysical Research*, *108*(B2). https://doi.org/10.1029/2002jb001778

Jaeger, J. C., & Cook, N. G. (1979). *Fundamentals of rock mechanics*. Chapman and Hall.

Jones, R. R., Pearce, M. A., Jacquemyn, C., & Watson, F. E. (2016). Robust best-fit planes from geospatial data. *Geosphere*, *12*(1), 196–202. https://doi.org/10.1130/GES01247.1

Kamer, Y., Ouillon, G., & Sornette, D. (2020). Fault network reconstruction using agglomerative clustering: Applications to southern Californian seismicity. *Natural Hazards and Earth System Sciences*, *20*(12), 3611–3625. https://doi.org/10.5194/nhess-20-3611-2020

Kastrup, U., Zoback, M. L., Deichmann, N., Evans, K. F., Giardini, D., & Michael, A. J. (2004). Stress field variations in the Swiss Alps and the northern Alpine foreland derived from inversion of fault plane solutions. *Journal of Geophysical Research*, *109*(B1), 1–22. https://doi.org/10.1029/2003jb002550

Kaven, J. O., & Pollard, D. D. (2013). Geometry of crustal faults: Identification from seismicity and implications for slip and stress transfer models. *Journal of Geophysical Research: Solid Earth*, *118*(9), 5058–5070. https://doi.org/10.1002/jgrb.50356

Kent, J. T. (1982). The Fisher-Bingham distribution on the sphere. *Journal of the Royal Statistical Society B*, *44*(1), 71–80. https://doi.org/10.1111/j.2517-6161.1982.tb01189.x

Kim, Y. S., Peacock, D. C. P., & Sanderson, D. J. (2004). Fault damage zones. *Journal of Structural Geology*, *26*(3), 503–517. https://doi.org/10.1016/j.jsg.2003.08.002

Kinoshita, M., Shiraishi, K., Demetriou, E., Hashimoto, Y., & Lin, W. (2019). Geometrical dependence on the stress and slip tendency acting on the subduction megathrust of the Nankai seismogenic zone off Kumano. *Progress in Earth and Planetary Science*, *6*(1), 7. https://doi.org/10.1186/s40645-018-0253-y

Lay, T., & Kanamori, H. (1981). Reprinted from earthquake prediction-An International review Maurice Ewing Series 4 copyright © 1981 by the American Geophysical Union. *Earthquake Prediction - An International Review*.

Lee, T., Diehl, T., Kissling, E., & Wiemer, S. (2023). New insights into the Rhône–Simplon fault system (Swiss Alps) from a consistent earthquake catalogue covering 35 yr. *Geophysical Journal International*, *232*(3), 1568–1589. https://doi.org/10.1093/gji/ggac407

Legrand, D., Marroquín, G., DeMets, C., Mixco, L., García, A., Villalobos, M., et al. (2020). Active deformation in the San Salvador extensional stepover, El Salvador from an analysis of the April–May 2017 earthquake sequence and GPS data. *Journal of South American Earth Sciences*, *104*(August), 102854. https://doi.org/10.1016/j.jsames.2020.102854

Leonard, M. (2010). Earthquake fault scaling: Self-consistent relating of rupture length, width, average displacement, and moment release. *Bulletin of the Seismological Society of America*, *100*(5 A), 1971–1988. https://doi.org/10.1785/0120090189

Leonard, M. (2014). Self-consistent earthquake fault-scaling relations: Update and extension to stable continental strike-slip faults. *Bulletin of the Seismological Society of America*, *104*(6), 2953–2965. https://doi.org/10.1785/0120140087

Levato, L., Sellami, S., Epard, J. L., Pruniaux, B., Olivier, R., Wagner, J. J., & Masson, H. (1994). The cover-basement contact beneath the Rawil axial depression (Western Alps): True amplitude seismic processing, petrophysical properties, and modelling. *Tectonophysics*, *232*(1–4), 391–409. https://doi.org/10.1016/0040-1951(94)90099-X

Lohman, R. B., & McGuire, J. J. (2007). Earthquake swarms driven by aseismic creep in the Salton Trough, California. *Journal of Geophysical Research*, *112*(B4), B04405. https://doi.org/10.1029/2006JB004596

Lomax, A., Michelini, A., & Curtis, A. (2014). Encyclopedia of complexity and systems science. *Encyclopedia of Complexity and Systems Science*. https://doi.org/10.1007/978-3-642-27737-5

Lomax, A., & Savvaidis, A. (2022). High-precision earthquake location using source-specific station terms and inter-event waveform similarity. *Journal of Geophysical Research: Solid Earth*, *127*, 1–28. https://doi.org/10.1029/2021jb023190

Lomax, A., Virieux, J., Volant, P., & Berge-Thierry, C. (2000). Probabilistic earthquake location in 3D and layered models (pp. 101–134). https://doi.org/10.1007/978-94-015-9536-0_5

Lynn, H., & Deregowski, S. (1981). Dip limitations on migrated sections as a function of line length and recording time. *Geophysics*, *46*(10), 1392–1397. https://doi.org/10.1190/1.1441146

Malservisi, R., Gans, C., & Furlong, K. P. (2003). Numerical modeling of strike-slip creeping faults and implications for the Hayward fault, California. *Tectonophysics*, *361*(1–2), 121–137. https://doi.org/10.1016/S0040-1951(02)00587-5

Mancktelow, N. (1985). The Simplon line: A major displacement zone in the Western Lepontine Alps. *Eclogae Geologicae Helvetiae*, *78*(1), 73–96.

Manighetti, I., Campillo, M., Bouley, S., & Cotton, F. (2007). Earthquake scaling, fault segmentation, and structural maturity. *Earth and Planetary Science Letters*, *253*(3–4), 429–438. https://doi.org/10.1016/j.epsl.2006.11.004

Manighetti, I., Mercier, A., & De Barros, L. (2021). Fault trace corrugation and segmentation as a measure of fault structural maturity. *Geophysical Research Letters*, *48*(20), e2021GL095372. https://doi.org/10.1029/2021GL095372

Manighetti, I., Zigone, D., Campillo, M., & Cotton, F. (2009). Self-similarity of the largest-scale segmentation of the faults: Implications for earthquake behavior. *Earth and Planetary Science Letters*, *288*(3–4), 370–381. https://doi.org/10.1016/j.epsl.2009.09.040

Mardia, K. V., & Jupp, P. E. (2000). Statistics of directional data (2nd ed.).

Martínez-Garzón, P., Ben-Zion, Y., Abolfathian, N., Kwiatek, G., & Bohnhoff, M. (2016). A refined methodology for stress inversions of earthquake focal mechanisms. *Journal of Geophysical Research: Solid Earth*, *121*(12), 8666–8687. https://doi.org/10.1002/2016JB013493

Maurer, H., Burkhard, M., Deichmann, N., & Green, A. G. (1997). Active tectonism in the Central Alps: Contrasting stress regimes north and south of the Rhone Valley. *Terra Nova*, *9*(2), 91–94. https://doi.org/10.1111/j.1365-3121.1997.tb00010.x

Meyer, S. G., Bassom, A. P., & Reading, A. M. (2019). Delineation of fault segments in mines using seismic source mechanisms and location uncertainty. *Journal of Applied Geophysics*, *170*, 103828. https://doi.org/10.1016/j.jappgeo.2019.103828

Moreno, M., Rosenau, M., & Oncken, O. (2010). 2010 Maule earthquake slip correlates with pre-seismic locking of Andean subduction zone. *Nature*, *467*(7312), 198–202. https://doi.org/10.1038/nature09349

Morris, A., Ferrill, D. A., & Henderson, D. B. (1996). Slip-tendency analysis and fault reactivation. *Geology*, *24*(3), 275–278. https://doi.org/10.1130/0091-7613(1996)024<0275:STAAFR>2.3.CO;2

Mousavi, S. M., Ellsworth, W. L., Zhu, W., Chuang, L. Y., & Beroza, G. C. (2020). Earthquake transformer—An attentive deep-learning model for simultaneous earthquake detection and phase picking. *Nature Communications*, *11*(1), 1–12. https://doi.org/10.1038/s41467-020-17591-w

Oglesby, D. D. (2005). The dynamics of strike-slip step-overs with linking dip-slip faults. *Bulletin of the Seismological Society of America*, *95*(5), 1604–1622. https://doi.org/10.1785/0120050058

Ouillon, G., Ducorbier, C., & Sornette, D. (2008). Automatic reconstruction of fault networks from seismicity catalogs: Three-dimensional optimal anisotropic dynamic clustering. *Journal of Geophysical Research*, *113*(1), 1–15. https://doi.org/10.1029/2007JB005032

Ouillon, G., & Sornette, D. (2011). Segmentation of fault networks determined from spatial clustering of earthquakes. *Journal of Geophysical Research*, *116*(2), 1–30. https://doi.org/10.1029/2010JB007752

Peacock, D. C. P., & Sanderson, D. J. (1995). Strike-slip relay ramps. *Journal of Structural Geology*, *17*(10), 1351–1360. https://doi.org/10.1016/0191-8141(95)97303-W

Pedregosa, F., Varoquaux, G., Gramfort, A., Michel, V., & Thirion, B. (2011). Scikit-learn: Machine learning in Python. *Journal of Machine Learning Research*, *12*, 2825–2830. https://doi.org/10.1289/EHP4713

Pennacchioni, G., & Mancktelow, N. S. (2013). Initiation and growth of strike-slip faults within intact metagranitoid (Neves area, Eastern Alps, Italy). *Bulletin of the Geological Society of America*, *125*(9–10), 1468–1483. https://doi.org/10.1130/B30832.1

Perrin, C., Manighetti, I., Ampuero, J. P., Cappa, F., & Gaudemer, Y. (2016). Location of largest earthquake slip and fast rupture controlled by along-strike change in fault structural maturity due to fault growth. *Journal of Geophysical Research: Solid Earth*, *121*(5), 3666–3685. https://doi.org/10.1002/2015JB012671

Petersen, G. M., Niemz, P., Cesca, S., Mouslopoulou, V., & Bocchini, G. M. (2021). Clusty, the waveform-based network similarity clustering toolbox: Concept and application to image complex faulting offshore Zakynthos (Greece). *Geophysical Journal International*, *224*(3), 2044–2059. https://doi.org/10.1093/gji/ggaa568

Pfiffner, O. A., Sahli, S., & Stäuble, M. (1997). Structure and evolution of the external basement massifs (Aar, Aiguilles-Rouges/Mt. Blanc). *Deep Structure of the Swiss Alps-Results from NRP*, *20*, 139–153.

Plotly Technologies. (2015). *Collaborative data science*. Montréal: Plotly Technologies Inc.

Poupinet, G., Ellsworth, W., & Frechet, J. (1984). Monitoring velocity variations in the crust using earthquake doublets: An application to the Calaveras Fault, California. *Journal of Geophysical Research*, *89*(B7), 5719–5731. https://doi.org/10.1029/JB089iB07p05719

Qiu, Q., Hill, E. M., Barbot, S., Hubbard, J., Feng, W., Lindsey, E. O., et al. (2016). The mechanism of partial rupture of a locked megathrust: The role of fault morphology. *Geology*, *44*(10), 875–878. https://doi.org/10.1130/G38178.1

Ramsay, J. G. (1981). Tectonics of the Helvetic Nappes. *Thrust and Nappe Tectonics*.

Ramsay, J. G. (1989). Fold and fault geometry in the Western Helvetic nappes of Switzerland and France and its implication for the evolution of the arc of the Western Alps. *Geological Society - Special Publications*, *45*(45), 33–45. https://doi.org/10.1144/GSL.SP.1989.045.01.02

Roland, E., & McGuire, J. J. (2009). Earthquake swarms on transform faults. *Geophysical Journal International*, *178*(3), 1677–1690. https://doi.org/10.1111/j.1365-246X.2009.04214.x

Romanet, P., Bhat, H. S., Jolivet, R., & Madariaga, R. (2018). Fast and slow slip events emerge due to fault geometrical complexity. *Geophysical Research Letters*, *45*(10), 4809–4819. https://doi.org/10.1029/2018GL077579

Ross, Z. E., Cochran, E. S., Trugman, D. T., & Smith, J. D. (2020). 3D fault architecture controls the dynamism of earthquake swarms. *Science*, *368*(6497), 1357–1361. https://doi.org/10.1126/science.abb0779

Ross, Z. E., Hauksson, E., & Ben-Zion, Y. (2017). Abundant off-fault seismicity and orthogonal structures in the San Jacinto fault zone. *Science Advances*, *3*(3). https://doi.org/10.1126/sciadv.1601946

Ross, Z. E., Trugman, D. T., Hauksson, E., & Shearer, P. M. (2019). Searching for hidden earthquakes in Southern California. *Science*, *771*(May), 767–771. https://doi.org/10.1126/science.aaw6888

Schaff, D. P., & Waldhauser, F. (2010). One magnitude unit reduction in detection threshold by cross correlation applied to parkfield (California) and China seismicity. *Bulletin of the Seismological Society of America*, *100*(6), 3224–3238. https://doi.org/10.1785/0120100042

Segall, P., & Pollard, D. D. (1980). Mechanics of discontinuous faults. *Journal of Geophysical Research*, *85*(B8), 4337–4350. https://doi.org/10.1029/jb085ib08p04337

Shakarji, C. M. (1998). Least-squares fitting algorithms of the NIST algorithm testing system. *Journal of Research of the National Institute of Standards and Technology*, *103*(6), 633–641. https://doi.org/10.6028/jres.103.043

Shelly, D. R. (2015). Complexity of the deep San Andreas Fault zone defined by cascading tremor. *Nature Geoscience*, *8*(2), 145–151. https://doi.org/10.1038/ngeo2335

Shelly, D. R., Beroza, G. C., Ide, S., & Nakamula, S. (2006). Low-frequency earthquakes in Shikoku, Japan, and their relationship to episodic tremor and slip. *Nature*, *442*(7099), 188–191. https://doi.org/10.1038/nature04931

Shi, P., Grigoli, F., Lanza, F., Beroza, G. C., Scarabello, L., & Wiemer, S. (2022). MALMI: An automated earthquake detection and location workflow based on machine learning and waveform migration. *Seismological Research Letters*, *93*(5), 2467–2483. https://doi.org/10.1785/0220220071

Sibson, R. H. (1983). Continental fault structure and the shallow earthquake source. *Journal of the Geological Society*, *140*(5), 741–767. https://doi.org/10.1144/gsjgs.140.5.0741

Sibson, R. H. (1986). Rupture interaction with Fault Jogs. In S. Das, J. Boatwright, & C. H. Scholz (Eds.), *Earthquake source mechanics*. https://doi.org/10.1029/GM037p0157

Sibson, R. H. (2014). Earthquake rupturing in fluid-overpressured Crust: How common? *Pure and Applied Geophysics*, *171*(11), 2867–2885. https://doi.org/10.1007/s00024-014-0838-3

Sibson, R. H. (2020). Preparation zones for large crustal earthquakes consequent on fault-valve action. *Earth Planets and Space*, *72*(31), 31. https://doi.org/10.1186/s40623-020-01153-x

Simon, V., Kraft, T., Diehl, T., & Tormann, T. (2021). Possible precursory slow-slip to two M L ~3 mainevents of the diemtigen microearthquake sequence, Switzerland. *Geophysical Research Letters*, *48*(19). https://doi.org/10.1029/2021gl093783

Skoumal, R. J., Ole Kaven, J., & Walter, J. I. (2019). Characterizing seismogenic fault structures in Oklahoma using a relocated template-matched catalog. *Seismological Research Letters*, *90*(4), 1535–1543. https://doi.org/10.1785/0220190045

Steck, A., Epard, J.-L., Escher, A., Lehner, P., Marchant, R., & Masson, H. (1997). Geological interpretation of the seismic profiles through Western Switzerland: Rawil (W1), Val d'Anniviers (W2), Mattertal (W3), Zmutt-Zermatt-Findelen (W4) and Val de Bagnes (W5). *Deep Structure of the Swiss Alps-Results from NRP*, *20*, 123–137.

Stein, S., & Wysession, M. (2003). An introduction to seismology, earthquakes, and Earth structure. https://doi.org/10.1029/2003eo220007

Swanson, M. T. (1988). Pseudotachylyte-bearing strike-slip duplex structures in the Fort Foster Brittle Zone, S. Maine. *Journal of Structural Geology*, *10*(8), 813–828. https://doi.org/10.1016/0191-8141(88)90097-1

Swanson, M. T. (2005). Geometry and kinematics of adhesive wear in brittle strike-slip fault zones. *Journal of Structural Geology*, *27*(5), 871–887. https://doi.org/10.1016/j.jsg.2004.11.009

Swisstopo, Federal Office of Topography. (2005). *Tectonic map of Switzerland 1:500'000*. Wabern.

Sylvester, A. G. (1988). Strike-slip faults. *Geological Society of America Bulletin*, *100*(11), 1666–1703. https://doi.org/10.1130/0016-7606(1988)100<1666:ssf>2.3.co;2

Theunissen, T., Chevrot, S., Sylvander, M., Monteiller, V., Calvet, M., Villaseñor, A., et al. (2018). Absolute earthquake locations using 3-D versus 1-D velocity models below a local seismic network: Example from the Pyrenees. *Geophysical Journal International*, *212*(3), 1806–1828. https://doi.org/10.1093/gji/ggx472

Trugman, D. T., & Shearer, P. M. (2017). GrowClust: A hierarchical clustering algorithm for relative earthquake relocation, with application to the Spanish Springs and Sheldon, Nevada, earthquake sequences. *Seismological Research Letters*, *88*(2), 379–391. https://doi.org/10.1785/0220160188

Truttmann, S., Diehl, T., & Herwegh, M. (2023a). Hypocenter-based 3D imaging of active faults: Method and applications in the southwestern Swiss Alps. [Dataset]. Zenodo. https://doi.org/10.5281/zenodo.7855039

Truttmann, S., Diehl, T., & Herwegh, M. (2023b). hypo_fault_imaging: April 22, 2023 Release (v0.1.1). [Software]. Zenodo. https://doi.org/10.5281/zenodo.7854999

Valoroso, L., Chiaraluce, L., Piccinini, D., Di Stefano, R., Schaff, D., & Waldhauser, F. (2013). Radiography of a normal fault system by 64,000 high-precision earthquake locations: The 2009 L'Aquila (central Italy) case study. *Journal of Geophysical Research: Solid Earth*, *118*(3), 1156–1176. https://doi.org/10.1002/jgrb.50130

Vavryčuk, V. (2014). Iterative joint inversion for stress and fault orientations from focal mechanisms. *Geophysical Journal International*, *199*(1), 69–77. https://doi.org/10.1093/gji/ggu224

Vavryčuk, V., Bouchaala, F., & Fischer, T. (2013). High-resolution fault image from accurate locations and focal mechanisms of the 2008 swarm earthquakes in West Bohemia, Czech Republic. *Tectonophysics*, *590*, 189–195. https://doi.org/10.1016/j.tecto.2013.01.025

Vidale, J. E., & Shearer, P. M. (2006). A survey of 71 earthquake bursts across southern California: Exploring the role of pore fluid pressure fluctuations and aseismic slip as drivers. *Journal of Geophysical Research*, *111*(B5), B05312. https://doi.org/10.1029/2005JB004034

Waldhauser, F., & Ellsworth, W. L. (2000). A double-difference earthquake location algorithm: Method and application to the Northern Hayward Fault, California. *Bulletin of the Seismological Society of America*, *90*(6), 1353–1368. https://doi.org/10.1785/0120000006

Wang, Y., Ouillon, G., Woessner, J., Sornette, D., & Husen, S. (2013). Automatic reconstruction of fault networks from seismicity catalogs including location uncertainty. *Journal of Geophysical Research: Solid Earth*, *118*(11), 5956–5975. https://doi.org/10.1002/2013JB010164

Wells, D. L., & Coppersmith, K. J. (1994). New empical relationship between magnitude, rupture length, rupture width, rupture area, and surface displacement. *Bulletin of the Seismological Society of America*, *84*(4), 974–1002.

Wibberley, C. A. J., Yielding, G., & Di Toro, G. (2008). Recent advances in the understanding of fault zone internal structure: A review. *Geological Society, London, Special Publications*, *299*(1), 5–33. https://doi.org/10.1144/SP299.2

Woodcock, N. H., & Fischer, M. (1986). Strike-slip duplexes. *Journal of Structural Geology*, *8*(7), 725–735. https://doi.org/10.1016/0191-8141(86)90021-0

Yuan, T. (2021). The 8-parameter Fisher–Bingham distribution on the sphere. *Computational Statistics*, *36*(1), 409–420. https://doi.org/10.1007/s00180-020-01023-w

Zhu, W., & Beroza, G. C. (2019). PhaseNet: A deep-neural-network-based seismic arrival-time picking method. *Geophysical Journal International*, *216*(1), 261–273. https://doi.org/10.1093/gji/ggy423

References From the Supporting Information

Diehl, T., Deichmann, N., Clinton, J., Kästli, P., Cauzzi, C., Kraft, T., et al. (2015). Earthquakes in Switzerland and surrounding regions during 2014. *Swiss Journal of Geosciences*, *108*(2–3), 425–443. https://doi.org/10.1007/s00015-015-0204-1